Post-Print

This is the accepted version of:

P. Xiao, L. Bin, R. Vescovini, S. Zheng
Optimal Design of Composite Sandwich Panel with Auxetic Reentrant Honeycomb Using Asymptotic Equivalent Model and PSO Algorithm
Composite Structures, Vol. 328, 2024, 117761 (15 pages)
doi:10.1016/j.compstruct.2023.117761

Optimal design of composite sandwich panel with auxetic reentrant honeycomb using asymptotic equivalent model and PSO algorithm

Peng Xiao[a,1,*], Lei Bin[a], Riccardo Vescovini[b], Shi Zheng[c]

[a]*School of Infrastructure Engineering, Nanchang University, Nanchang 330031, China*
[b]*Dipartimento di Scienze e Tecnologie Aerospaziali, Politecnico di Milano, Milano 20156, Italy*
[c]*School of Civil and Resource Engineering, University of Science and Technology Beijing, Beijing 100083, China*

Abstract

The composite honeycomb sandwich with auxetic reentrant honeycomb (CSP-ARH) is a typical negative Poisson's ratio structure, which has better mechanical properties than composite structure with positive Poisson's ratio. In this study, a 2D asymptotic equivalent model (AEM) based on the variational asymptotic method (VAM) is proposed and used to analyze the vibration, buckling, and optimization problems of CSP-ARH incorporating CFRP facesheets and an aluminum honeycomb core. Comparative analyses with 3D finite element results demonstrate the exact and efficient analysis of the buckling and free vibration characteristics of CSP-ARH using this method. Subsequently, a particle swarm optimization (PSO) algorithm can be applied to optimize the mesoscopic size of composite facesheets and honeycomb core. The primary objectives of the optimization process involve maximizing the buckling load and natural frequency, or alternatively, minimizing the mass while satisfying specific mechanical properties requirements. Moreover, a few additional optimization iterations are performed to find the optimal shape coefficients of the curved fibers in the CFRP facesheets for variable stiffness composite sandwich panels. The shape of the curved fiber is defined using a cubic polynomial function $f(x, y)$ and is described by a 20×20 grid of discrete elements. The results indicate that CSP-ARH with optimal curved fibers shapes exhibit superior performance compared to those with straight fibers, with buckling load and natural frequency increased by 8.18% and 7.09%, respectively.

☆This paper is contributed by all authors
*Corresponding author.
Email address: pengxiao@ncu.edu.cn (Peng Xiao)
[1]+86 13866104225

Keywords: Variational asymptotic method, Reentrant honeycomb, Buckling, Free vibration, Particle swarm optimization

---

Nomenclature

$\bar{\lambda}_i$ Lagrangian multipliers

$\bar{\omega}$ non-dimensional frequency

$\boldsymbol{R}$ strains measures of Reissner-Mindlin plate

$\langle\cdot\rangle$ volume average over the unit cell

ω_1 fundamental frequency

ρ^* equivalent density

τ_i, β_i traction forces on the upper and lower surface

θ cell angle of core

θ_i fiber ply angle

θ_{np} fiber orientation angle within the unit

$\tilde{\boldsymbol{v}}$, v_3 in-plane and out-of-plane perturbation warping functions

c_{ij} fiber shape factor

h_c thickness of core

w_i warping functions

x_i, y_i macro- and micro-coordinates

$X^k_{i,pbest}(j)$, $X^k_{i,gbest}(j)$ local and global optimal positions

$\bar{\omega}_{\text{opt}}$ non-dimensional fundamental frequency optimal solution

$\overline{\delta W}_{2D}, \overline{\delta W}^*$ virtual work independent of and relevant to warping functions

f_i body force per unit volume

$h_{\mathrm{i,j}}(x)$ constraint function

h height of the panel

$N_{x_1,avg}$ boundary mean surface force

P_{opt}, ω_{opt} critical buckling load optimal solution

$X_{\mathbf{i}}(j)$, $V_{\mathbf{i}}(j)$ particle position and velocity vectors

1. Introduction

Composite honeycomb sandwich panels have gained considerable attention in the field of lightweight engineering owing to their exceptional impact resistance, high strength, and design flexibility [1, 2]. Honeycomb sandwich panels are made of two highly rigid sheets bonded to a honeycomb core material with lower strength and stiffness. By varying the thickness and material of the core as well as the panels, a variety of properties and desired performance can be obtained. Several types of core shapes and core materials have been applied in the construction of sandwich structures [3, 4]. Honeycomb cores are described as s cellular solids, that make use of voids to decrease mass, whilst maintaining qualities of stiffness and energy absorption [5]. In recent years, advancements in mechanical metamaterials have enabled the deliberate manipulation of the physical properties of original materials through the design of internal structures [6]. This has allowed for the emergence of unique mechanical phenomena, such as negative Poisson's ratio (NPR). Unlike traditional structures, NPR structures exhibit lateral expansion when subjected to axial tension, displaying the counterintuitive auxetic behavior. This unusual auxetic behavior imparts NPR honeycomb sandwich panels with enhanced impact and fracture resistance capabilities [7, 8, 9], thus presenting extensive prospects in aerospace, civil engineering, and other fields.

Extensive studies have been conducted on the buckling and vibration behaviors of conventional honeycomb strucutures, encompassing theoretical analysis, finite element software simulation, and experimental investigations. Frostig et al. [10] proposed the high-order sandwich panel theory (HSAPT), which utilizes the Euler-Bernoulli beam to model the skins and two-dimensional elastic theory for the core. Phan et al. [11] further enhanced HSAPT by incorporating the in-plane stiffness of the core and demonstrated its improved accuracy in predicting buckling, surpassing the previous HSAPT models [12, 13].

Shi and Tong [14] evaluated the local buckling of honeycomb sandwich panels subjected to lateral loads. They employed the two-scale homogenization method for periodic media to compute these forces. Rais-Rohani and Marcellier [15] utilized the small-deflection theory to investigat the buckling and free vibration behaviors of rectangular sandwich panels and solved the corresponding eigenvalue problems using the Rayleigh-Ritz method. In Ref [16], the third-order polynomial displacement model is introduced into the simplified isoparametric assumed FE formulation for buckling and vibration analysis of composite sandwich panels. Liu et al. [17] applied Fourier series and Galerkin method to develop a closed-form solution, which can be used in the analysis of various mechanical properties of simply-supported honeycomb sandwich panels. Wang et al. [18] presented a 2D equivalent model using the orthotropic constitutive relation of the layered composite honeycomb core and studied the vibration behaviors of sandwich plates by comparing them with the 3D finite element results.

The research on the buckling properties of reentrant honeycomb sandwich panels is relatively limited. Peng et al. [19] decoupled the original nonlinear model into a 2D geometrical nonlinear problem using the variational asymptotic method to solve the buckling problem of NPR honeycomb sandwich plates. Quang et al. [20] analyzed the nonlinear buckling of magneto-electro-elastic sandwich panels with NPR core under multi-field loads based on higher-order shear-deformed plate theory. This analysis considered the effects of geometric nonlinear. Sarafraz et al. [21] adopted the differential quadrature method (DQM) to perform uniaxial, biaxial, and shear buckling analyses on the NPR honeycomb sandwich panels.

Investigations regarding vibration problems, both forced and free, are also relatively limited. Scarpa and Tomlinson [22] explored re-entrant honeycombs using cellular material method, and applied the first-order sandwich panel theory to analyze fundamental frequencies. Based on Reddy's third-order shear deformation plate theory, Zhu et al. [23] studied the natural frequencies and energies for the NPR honeycomb sandwich panel, and obtained the variation trend of potential energies and total energies with respect to the plate's parameters. The free vibration problem of sandwich plates composed of re-entrant honeycomb core and FGM skins was solved by applying Navier's method in the work of Singh and Harsha [24]. Recently, Zhu et al. [25] adopted the third-order shear deformation theory to investigate the multiple periodic vibration responds of the re-entrant honeycomb sandwich panel under in-plane and transverse excitations, based on von Kármán type geometric nonlinear assumptions.

Despite extensive research on the buckling and vibration characteristics of honeycomb sandwich panels, limited attention has been given to optimizing these properties. A variety of algorithms had been used to conduct optimization analysis on composite and auxetic structures [26, 27, 28, 29]. Among them, the Particle Swarm Optimization (PSO) algorithm has been a widely adopted stochastic search heuristic algorithm since it was proposed in 1995 [30]. This algorithm mimics the foraging behavior of birds, where particles in the population incorporate personal best (pbest) and global best (gbest) information to explore the entire search space. By iteratively updating particle positions and velocities, the PSO algorithm aims to converge towards the optimal solution. Notably, the PSO algorithm offers advantages such as rapid convergence, a minimal number of parameters, and ease of implementation, rendering it applicable in diverse research domains. Marini and Walczak [31] provided a comprehensive introduction to the fundamental concepts, theories, and applications of the PSO algorithm.

Cho [32] conducted an optimization study aiming to improve the performance of laminates by utilizing three different material stacking sequences consisted of mixed plies and single-angle plies as design variables. The PSO algorithm, along with a specially developed finite element program, was employed to optimize these design variables. Mohammadian and Fereidoon [33] focused on the multi-objective optimization of open-prism sandwich plates, which involved applying the Multi-Objective Particle Swarm Optimization (MOPSO) algorithm to simultaneously achieve minimum weight and maximum heat transfer index. Gholami et al. [34] employed the PSO algorithm to optimize honeycomb sandwich panels with the objective of minimizing panel weight. The optimization took into account various factors and the results demonstrated the feasibility and efficiency of the PSO algorithm in obtaining optimal solutions for different types of objective functions.

Wang et al. [35] introduced a novel sandwich panel featuring a three-dimensional double-V auxiliary (DVA) structural core to achieve isotropic performance. To reduce dynamic response under blast loads and mass constraints, the parameters of the core optimization problem were optimized using the MOPSO algorithm, thereby validating the effectiveness of the optimization process. Feng et al. [36] conducted structural design and performance optimization of three-ply minimum-curvature sandwich panels, employing the Constrained Improved Particle Swarm Optimization (CIPSO) algorithm with the objective of achieving desired mechanical and structural performance. Vosoughi et al. [37, 38, 39, 40] introduced a hybrid algorithm combining finite elements (FE), genetic algorithms (GA) and PSO to find the optimal solution for thick laminated composite plate, hexagonal honeycomb sandwich panels and stiffened laminated composite panels to achieve their maximum buckling load. Related studies demonstrate the efficiency and accuracy of the proposed solution procedure and investigate the impact of different parameters on plate design optimization.

In this study, we aim to optimize the buckling loads and natural frequencis of reentrant honeycomb sandwich panels using the PSO algorithm. To accomplish this, we employ the Variational Asymptotic Method (VAM), an equivalent dimensionality reduction method, for homogenization analysis of this periodic structure. This analysis enables the batch calculation of mechanical properties for sandwich panels. Initially proposed by Cesnik and Hodges [41], VAM is based on the principle of asymptotic expansion. It expresses the solution to a problem as a series expansion in terms of a small parameter, and captured the dominant behavior by ignoring higher-order expansion terms.

The work by Yu and Hodge [42, 43] extended the application of the VAM to develop models for linear elastic composite structures, including laminated plates [19], shells [44], and beams [45]. By utilizing a unified formulation, VAM effectively incorporates geometric nonlinearity into these structural elements. Consequently, it serves as a powerful and efficient tool for the investigation and design of composite structures, maintaining a desirable balance between computational efficiency and accuracy.

Building upon the authors' previous research on the composite sandwich panel with auxetic reentrant honeycomb (CSP-ARH) [19, 46, 47], this study discusses the effect of structural parameters and NPR on the mechanical properties of CSP-ARH with straight fiber laminates using a VAM-based 2D asymptotic equivalent model (2D-AEM) [48, 49]. In addition, this work extends 2D-AEM to obtain the buckling and free vibration properties of CSP-ARH with curve fiber laminates (CSP-ARH-CFL), which offer variable stiffness properties to the facesheet. Fig. 1 depicts the workflow of equivalence and optimization analysis of CSP-ARH-CFL based on 2D-AEM. The combination of VAM and PSO for optimizing analysis of composite honeycomb sandwich panels has not been previously explored, which is innovative in the field of sandwich panel structure optimization.

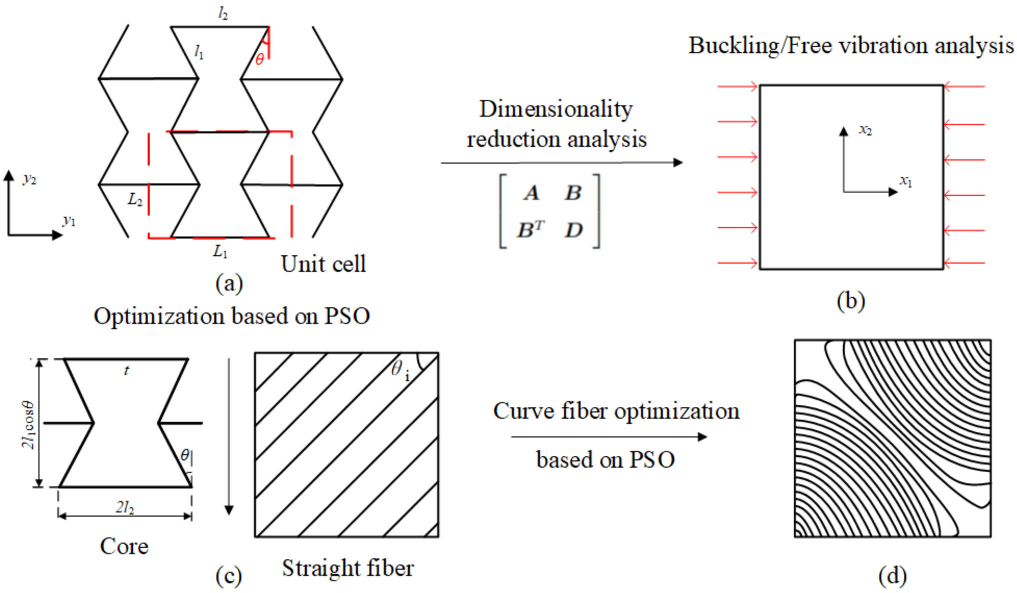

Figure 1: Flowchart for obtaining optimal buckling load and natural frequency of CSP-ARH using 2D-AEM and PSO algorithm: (a) unit cell; (b) buckling and free vibration analysis; (c) optimization of CSP-ARH; (d) optimization of CSP-ARH-CLF.

The subsequent sections of this article are organized into five parts. Section 2 applies VAM to analyze the equivalent performance of CSP-ARH for dimensionality reduction, and outlines the calculation procedures for analyzing the buckling and free vibration behaviors using 2D-AEM. The accuracy and feasibility of this model in predicting buckling loads and natural vibration frequencies are demonstrated by comparing is with the results obtained from 3D-FEM in section 3. Section 4 employs the PSO algorithm to optimize the structural performance of CSP-ARH by controlling the ply angle of each layer and the structural parameters of the core layer. The optimization aims to either maximize the buckling load and natural frequency, or minimize the mass of the panel while satisfying specific performance criteria. Furthermore, Section 5 incorporates the optimization results of CSP-ARH into the optimization problem of the curved fiber shape in CSP-ARH-CFL. The curved fiber is represented by a cubic polynomial function, with the coefficient of each term serving as design variables. Finally, Section 6 listed the conclusions of this study. In general, this study adopts VAM to reduce the dimensionality of the model containing deterministic parameters, and then brings the asymptotic equivalent model into the overall model to optimize the uncertain parameters. On the premise of meeting a certain accuracy, the calculation efficiency is greatly improved compared with the traditional approach.

2. Dimensionality reduction formulation

2.1. Potential energy of CSP-ARH

In the asymptotically equivalent model, the field variables of CSP-ARH is represented using the local coordinates y_i $(i = 1, 2, 3)$ and global coordinates x_α $(\alpha = 1, 2)$ as [42]

$$\frac{\partial f\left(x_\alpha, y_i, t\right)}{\partial x_\alpha} = \left.\frac{\partial f\left(x_\alpha, y_i, t\right)}{\partial x_\alpha}\right|_{y_i=const} + \frac{1}{\zeta}\left.\frac{\partial f\left(x_\alpha, y_i, t\right)}{\partial y_i}\right|_{x_\alpha=const} \equiv f_{,\alpha} + \frac{1}{\zeta} f_{;i}, \tag{1}$$

where the axis x_3 is disregarded; ζ $(\zeta = x_i/y_i)$ represents the small parameter.

The displacement variables of 3D plate u_i is able to split into 2D plate variables $\bar{u}_i$ and warping function w_i as follows

$$\begin{aligned}
u_1\left(x_\alpha, y_i, t\right) &= \underline{\bar{u}_1\left(x_\alpha, t\right) - \zeta y_3 \bar{u}_{3,1}\left(x_\alpha, t\right)} + \zeta w_1\left(x_\alpha, y_i, t\right),\\
u_2\left(x_\alpha, y_i, t\right) &= \underline{\bar{u}_2\left(x_\alpha, t\right) - \zeta y_3 \bar{u}_{3,2}\left(x_\alpha, t\right)} + \zeta w_2\left(x_\alpha, y_i, t\right),\\
u_3\left(x_\alpha, y_i, t\right) &= \underline{\bar{u}_3\left(x_\alpha, t\right)} + \zeta w_3\left(x_\alpha, y_i, t\right),
\end{aligned} \tag{2}$$

where the underlined terms are the deformations of the reference surface, and must adhere to the constraints

$$h\bar{u}_a\left(x_a\right) = \left\langle u_a\right\rangle + \left\langle \zeta y_3\right\rangle \bar{u}_{3,2}, \quad h\bar{u}_3\left(x_\alpha\right) = \left\langle u_3\right\rangle, \tag{3}$$

The warping functions are restricted by

$$\left\langle w_i\right\rangle = 0. \tag{4}$$

Strain can be expressed as

$$\varepsilon_{ij} = \frac{1}{2}\left(\frac{\partial u_i}{\partial x_j} + \frac{\partial u_j}{\partial x_i}\right). \tag{5}$$

Substituting Eq. (2) into Eq. (5) gives

$$
\begin{aligned}
\varepsilon_{11} &= \epsilon_{11} + \zeta y_3 \kappa_{11} + w_{1;1}, \\
2\varepsilon_{12} &= 2\epsilon_{12} + 2\zeta y_3 \kappa_{12} + w_{1,2} + w_{2;1}, \\
\varepsilon_{22} &= \epsilon_{22} + \zeta y_3 \kappa_{22} + w_{2;2}, \\
2\varepsilon_{13} &= w_{1;3} + w_{3;1}, \\
2\varepsilon_{23} &= w_{2;3} + w_{3;2}, \\
\varepsilon_{33} &= w_{3;3},
\end{aligned} \tag{6}
$$

where $\epsilon_{\alpha\beta}$ and $\kappa_{\alpha\beta}$ is expressed as

$$
\epsilon_{\alpha\beta}\left(x_1, x_2\right) = \frac{1}{2}\left(\bar{u}_{\alpha,\beta} + \bar{u}_{\beta,\alpha}\right), \quad \kappa_{\alpha\beta}\left(x_1, x_2\right) = -\bar{u}_{3,\alpha\beta}. \tag{7}
$$

The 3D strain field is defined as []

$$
\begin{aligned}
&\boldsymbol{\mathcal{E}}_e = \left[\varepsilon_{11} \quad \varepsilon_{22} \quad 2\varepsilon_{12}\right]^{\mathrm{T}} = \boldsymbol{\epsilon} + \zeta y_3 \boldsymbol{\kappa} + \boldsymbol{I}_\alpha \boldsymbol{w}_{||;\alpha}, \\
&2\boldsymbol{\mathcal{E}}_s = \left[2\varepsilon_{13} \quad 2\varepsilon_{23}\right]^{\mathrm{T}} = \boldsymbol{w}_{||;3} + \boldsymbol{e}_\alpha w_{3;\alpha}, \\
&\mathcal{E}_t = \varepsilon_{33} = w_{3;3},
\end{aligned} \tag{8}
$$

where $()_{||} = \left[()_1 \quad ()_2\right]^{\mathrm{T}}$, $\boldsymbol{\epsilon} = \left[\begin{array}{ccc} \epsilon_{11} & 2\epsilon_{12} & \epsilon_{22} \end{array}\right]^{\mathrm{T}}$, $\boldsymbol{\kappa} = \left[\kappa_{11} \quad \kappa_{12}+\kappa_{21} \quad \kappa_{22}\right]^{\mathrm{T}}$, and

$$
\boldsymbol{I_1} = \left[\begin{array}{cc} 1 & 0 \\ 0 & 1 \\ 0 & 0 \end{array}\right], \boldsymbol{I_2} = \left[\begin{array}{cc} 0 & 0 \\ 1 & 0 \\ 0 & 1 \end{array}\right], \boldsymbol{e}_1 = \left\{\begin{array}{c} 1 \\ 0 \end{array}\right\}, \boldsymbol{e}_2 = \left\{\begin{array}{c} 0 \\ 1 \end{array}\right\}. \tag{9}
$$

The strain energy of CSP-ARH is expressed as

$$
U = \frac{1}{2}\int_{-a/2}^{a/2}\int_{-b/2}^{b/2} \frac{1}{\Omega} U_\Omega \mathrm{d}x_2 \mathrm{d}x_1 \tag{10}
$$

Eq. (10) can be expressed as

$$
U = \frac{1}{2}\left\langle \boldsymbol{\mathcal{E}}^{\mathrm{T}} \boldsymbol{D} \boldsymbol{\mathcal{E}} \right\rangle = \frac{1}{2}\left\langle \left\{\begin{array}{c} \boldsymbol{\mathcal{E}}_e \\ 2\boldsymbol{\mathcal{E}}_s \\ \boldsymbol{\mathcal{E}}_t \end{array}\right\}^{\mathrm{T}} \left[\begin{array}{ccc} \boldsymbol{D}_e & \boldsymbol{D}_{es} & \boldsymbol{D}_{et} \\ \boldsymbol{D}_{es}^{\mathrm{T}} & \boldsymbol{D}_s & \boldsymbol{D}_{st} \\ \boldsymbol{D}_{et}^{\mathrm{T}} & \boldsymbol{D}_{st}^{\mathrm{T}} & \boldsymbol{D}_t \end{array}\right] \left\{\begin{array}{c} \boldsymbol{\mathcal{E}}_e \\ 2\boldsymbol{\mathcal{E}}_s \\ \boldsymbol{\mathcal{E}}_t \end{array}\right\} \right\rangle \tag{11}
$$

The external force virtual work is divided as

$$
\delta\overline{\mathcal{W}}_{3D} = \delta\overline{\mathcal{W}}_{2D} + \delta\overline{\mathcal{W}}^*, \tag{12}
$$

where $\delta\overline{\mathcal{W}}_{2D}$ and $\delta\overline{\mathcal{W}}^*$ represents the virtual work independent and related to w_i, and

$$
\delta\overline{\mathcal{W}}_{2D} = \int_s \left(p_i \delta\bar{u}_i + q_a \delta\bar{u}_{3,a}\right) ds, \quad \delta\overline{\mathcal{W}}^* = \int_s \left(\left\langle f_i \delta w_i \right\rangle + \tau_i \delta w_i^+ + \beta_i \delta w_i^-\right) ds, \tag{13}
$$

where $(\cdot)^+$ and $(\cdot)^-$ is the parameter of the upper and lower of the panel, respectively; τ_i, β_i, and f_i are the traction forces on the upper and lower surface of the panel and the body force, respectively; and $p_i = \langle f_i \rangle + a_i + \beta_i, q_a = h/2\,(\beta_a - a_a) - \langle x_3 f_a \rangle$.

The potential energy functional of CSP-ARH is written as

$$\delta \Pi = \delta U - \delta \overline{\mathcal{W}}_{3D} = 0 \tag{14}$$

2.2. Zero-order approximation

The determination of w_i can be achieved by employing an asymptotic solution of variation. Before that, it is necessary to first evaluate the order of each term in Eq. (14), such as [48]

$$\begin{aligned} &\epsilon_{\alpha\beta} \sim h\kappa_{\alpha\beta} \sim n, w_i \sim hn, \boldsymbol{w}_{\|;\alpha} \sim w_{3;\alpha} \sim \frac{h}{a} n \\ &\boldsymbol{w}_{\|;3} \sim w_{3;3} \sim n, hf_\alpha \sim \alpha_\alpha \sim \beta_\alpha \sim \mu \frac{h}{a} n, hf_3 \sim \alpha_3 \sim \beta_3 \sim \mu \left(\frac{h}{a}\right)^2 \end{aligned} \tag{15}$$

where n is the order of the minimum strain; and μ is the order of the material properties.

The potential energy functional of CSP-ARH is transformed into the form of the zeroth-order approximation by removing the asymptotically smaller terms $\delta \overline{\mathcal{W}}_{2D}$ in Eq. (15)

$$\delta \Pi = \delta U - \delta \overline{\mathcal{W}}^{*} = 0 \tag{16}$$

where zero-order approximate strain energy U_0 is obtained from Eq. (12) as

$$2U_0 = \left\langle \begin{array}{c} (\boldsymbol{\epsilon} + x_3\boldsymbol{\kappa})^{\mathrm{T}} \boldsymbol{D}_e (\boldsymbol{\epsilon} + x_3\boldsymbol{\kappa}) + w_{\|,3}^{\mathrm{T}} \boldsymbol{D}_s \boldsymbol{w}_{\|,3} + w_{3,3}^{\mathrm{T}} \boldsymbol{D}_t w_{3,3} \\ +2 (\boldsymbol{\epsilon} + x_3\boldsymbol{\kappa})^{\mathrm{T}} \left(\boldsymbol{D}_{es} \boldsymbol{w}_{\|,3} + \boldsymbol{D}_{et} w_{3,3}\right) + 2\boldsymbol{w}_{\|,3}^{\mathrm{T}} \boldsymbol{D}_{st} w_{3,3} \end{array} \right\rangle. \tag{17}$$

Due to the principle of minimum potential energy, w_i is solved from Eq. (4) and Eq. (16) as

$$\delta \left(\Pi + \Lambda_i \left\langle \langle \boldsymbol{w}_i \rangle \right\rangle \right) = 0 \tag{18}$$

The relevant Euler-Lagrange multipliers can be expressed as

$$\begin{aligned} &\left[(\boldsymbol{\epsilon} + x_3\boldsymbol{\kappa})^{\mathrm{T}} \boldsymbol{D}_{es} + \left(\boldsymbol{w}_{\|,3}\right)^{\mathrm{T}} \boldsymbol{D}_s + w_{3,3} \boldsymbol{D}_{st} \right]_{,3} = \bar{\boldsymbol{\lambda}}_{\|}, \\ &\left[(\boldsymbol{\epsilon} + x_3\boldsymbol{\kappa})^{\mathrm{T}} \boldsymbol{D}_{et} + \left(\boldsymbol{w}_{\|,3}\right)^{\mathrm{T}} \boldsymbol{D}_{st} + w_{3,3} \boldsymbol{D}_t \right]_{,3} = \bar{\lambda}_3, \end{aligned} \tag{19}$$

where $\bar{\boldsymbol{\lambda}}_{\|} = \begin{bmatrix} \bar{\lambda}_1 & \bar{\lambda}_2 \end{bmatrix}^{\mathrm{T}}$ and $\bar{\lambda}_3$ are Lagrange multipliers used to impose in-plane and out-of-plane constraints.

In accordance with the free surface condition, the constrains at the upper and lower surface of the plate is expressed as

$$\begin{aligned} \left[(\boldsymbol{\epsilon} + x_3 \boldsymbol{\kappa})^{\mathrm{T}} \boldsymbol{D}_{es} + \boldsymbol{w}_{\|,3}^{\mathrm{T}} \boldsymbol{D}_s + w_{3,3} \boldsymbol{D}_{st}^{\mathrm{T}} \right]^{+/-} &= 0, \\ \left[(\boldsymbol{\epsilon} + x_3 \boldsymbol{\kappa})^{\mathrm{T}} \boldsymbol{D}_{et} + \boldsymbol{w}_{\|,3}^{\mathrm{T}} \boldsymbol{D}_{st} + w_{3,3} \boldsymbol{D}_t \right]^{+/-} &= 0, \end{aligned} \tag{20}$$

where the "+/-" represent value at the upper and lower surfaces of the panel.

Substitute Eq. (20) into Eq. (18) gives

$$\boldsymbol{w}_{\|} = \left\langle - (\boldsymbol{\epsilon} + x_3 \boldsymbol{\kappa}) \overline{\boldsymbol{D}}_{es} (\boldsymbol{D}_s)^{-1} \right\rangle^{\mathrm{T}}, w_3 = \left\langle - (\boldsymbol{\epsilon} + x_3 \boldsymbol{\kappa}) \overline{\boldsymbol{D}}_{et} (\boldsymbol{D}_t)^{-1} \right\rangle, \tag{21}$$

where

$$\begin{aligned} &\overline{\boldsymbol{D}}_{es} = \boldsymbol{D}_{es} - \overline{\boldsymbol{D}}_{et} (\boldsymbol{D}_{st})^{\mathrm{T}} \left(\overline{\boldsymbol{D}}_t\right)^{-1}, \quad \overline{\boldsymbol{D}}_{et} = \boldsymbol{D}_{et} - \boldsymbol{D}_{es} (\boldsymbol{D}_s)^{-1} \boldsymbol{D}_{st}, \\ &\overline{\boldsymbol{D}}_t = \boldsymbol{D}_t - (\boldsymbol{D}_{st})^{\mathrm{T}} (\boldsymbol{D}_s)^{-1} \boldsymbol{D}_{st} \end{aligned} \tag{22}$$

Plug Eq. (21) into Eq. (17) gives

$$U_{2D} = \frac{1}{2} \left\langle (\boldsymbol{\epsilon} + x_3 \boldsymbol{\kappa})^{\mathrm{T}} K (\boldsymbol{\epsilon} + x_3 \boldsymbol{\kappa}) \right\rangle = \frac{1}{2} \left\{ \begin{array}{c} \boldsymbol{\epsilon} \\ \boldsymbol{\kappa} \end{array} \right\}^{\mathrm{T}} \left[\begin{array}{cc} \boldsymbol{A} & \boldsymbol{B} \\ \boldsymbol{B}^T & \boldsymbol{D} \end{array} \right] \left\{ \begin{array}{c} \boldsymbol{\epsilon} \\ \boldsymbol{\kappa} \end{array} \right\} \tag{23}$$

where

$$\begin{aligned} &\boldsymbol{A} = \left\langle \overline{\boldsymbol{D}}_e \right\rangle, \quad \boldsymbol{B} = \left\langle x_3 \overline{\boldsymbol{D}}_e \right\rangle, \quad \boldsymbol{D} = \left\langle x_3^2 \overline{\boldsymbol{D}}_e \right\rangle, \\ &\overline{\boldsymbol{D}}_e = \boldsymbol{D}_e - \overline{\boldsymbol{D}}_{es} \boldsymbol{D}_s^{-1} \boldsymbol{D}_{es}^{\mathrm{T}} - \overline{\boldsymbol{D}}_{et} \boldsymbol{D}_{et}^{\mathrm{T}} / \overline{\boldsymbol{D}}_t. \end{aligned} \tag{24}$$

2.3. First-order approximation

The zeroth-order energy approximation corresponds to the CLT, which merely provides in-plane stress information. In order to determine the out-of-plane stresses, the next higher-order term in the strain tensor must be taken into account. This consideration results in a more accurate estimation of the potential energy of CSP-ARH. The refined theory, also referred to as the first-order approximation of both the energy and the warping functions, is obtained through perturbing the zeroth-order warping functions as [49]

$$\tilde{\boldsymbol{w}}_{\|} = \boldsymbol{v}_{\|}, \quad \tilde{w}_3 = v_3 + \hat{\boldsymbol{D}} \chi \tag{25}$$

where $\boldsymbol{\chi} = \left[\begin{array}{cc} \boldsymbol{\epsilon} & \boldsymbol{\kappa} \end{array} \right]^{\mathrm{T}}$, $\hat{\boldsymbol{D}} = \left[\begin{array}{cc} \hat{D}_1 & \hat{D}_2 \end{array} \right]$, $\hat{D}_1' = -D_{\mathrm{et}}^{\mathrm{T}} / D_{\mathrm{t}}$, $\hat{D}_2' = -x_3 D_{\mathrm{et}}^{\mathrm{T}} / D_{\mathrm{t}}$, $\left\langle \hat{D}_\alpha \right\rangle = 0$; $\boldsymbol{v}_{\|}$ and v_3 are in-plane and out-of-plane perturbations of the warping fields to the first-order approximation, respectively.

Substitute Eq. (25) into Eq. (16), we obtain

$$\begin{aligned}&2\Pi_1=\left\langle \boldsymbol{v}_\parallel^{\mathrm{T}}\boldsymbol{D}_s\boldsymbol{v}_{\parallel,3}+\boldsymbol{D}_t\boldsymbol{v}_{3,3}^2+2\boldsymbol{v}_\parallel^{\mathrm{T}}\boldsymbol{C}_{\alpha,3}\chi_{,\alpha}+2\boldsymbol{v}_\parallel^{\mathrm{T}}\boldsymbol{D}_s\partial_t\hat{\boldsymbol{D}}_{,\alpha}-2\boldsymbol{v}_\parallel^{\mathrm{T}}\boldsymbol{f}_\parallel\right\rangle\\&-2\tilde{\boldsymbol{v}}_\parallel^{+\mathrm{T}}\boldsymbol{\tau}_\parallel-2\boldsymbol{v}_\parallel^{-\mathrm{T}}\boldsymbol{\beta}_\parallel\end{aligned}\tag{26}$$

where $\boldsymbol{C}_{\alpha,3}=-\partial_e^{\mathrm{T}}\left[\begin{array}{cc}\overline{\boldsymbol{D}}_e & x_3\overline{\boldsymbol{D}}_e\end{array}\right]$, $\partial_e=\left[\begin{array}{cc}(\cdot)_{,1} & 0\\ (\cdot)_{,2} & (\cdot)_{,1}\\ 0 & (\cdot)_{,2}\end{array}\right]$, $\partial_t=\left\{\begin{array}{c}(\cdot)_{,1}\\ (\cdot)_{,2}\end{array}\right\}$.

The Euler-Lagrange equation of Eq. (26) is

$$\delta\boldsymbol{v}_\parallel:\left(\boldsymbol{D}_s\boldsymbol{v}_{\parallel,3}+\boldsymbol{D}_s\partial_t\hat{\boldsymbol{D}}\boldsymbol{\chi}_{,\alpha}\right)_3=\boldsymbol{C}_{\alpha,3}\partial_t\hat{\boldsymbol{D}}\boldsymbol{\chi}_{,\alpha}-\boldsymbol{f}_\parallel+\boldsymbol{\Lambda}_\parallel\tag{27}$$

Based on Eq. (4) and Eq. (27), it can be deduced that v_3 is a trivial solution, and the disturbing warping function is expressed as

$$\boldsymbol{v}_\parallel=\overline{\boldsymbol{C}}_\alpha\boldsymbol{\chi}_{,\alpha}-\langle\overline{\boldsymbol{f}}\rangle\tag{28}$$

where

$$\begin{aligned}&\overline{\boldsymbol{C}}_{\alpha,3}=\boldsymbol{D}_s^{-1}\boldsymbol{C}_\alpha^*,\boldsymbol{C}_\alpha^*=\boldsymbol{C}_\alpha+\frac{x_3}{h}\boldsymbol{C}_\alpha^{\mp}-\frac{1}{2}\boldsymbol{C}_\alpha^{\pm}-\boldsymbol{D}_s\partial_t\hat{\boldsymbol{D}}\\&\overline{\boldsymbol{f}}=\boldsymbol{D}_s^{-1}\boldsymbol{f}^*,\boldsymbol{f}^*=\boldsymbol{f}+\frac{x_3}{h}\boldsymbol{f}^{\mp}-\frac{1}{2}\boldsymbol{f}^{\pm}+\left(\frac{x_3}{h}+\frac{1}{2}\right)\boldsymbol{\tau}_\parallel+\left(\frac{x_3}{h}-\frac{1}{2}\right)\boldsymbol{\beta}_\parallel\end{aligned}\tag{29}$$

with $(\cdot)^{\pm}=(\cdot)^{+}+(\cdot)^{-}$, $(\cdot)^{\mp}=(\cdot)^{-}-(\cdot)^{+}$.

The first-order asymptotically potential energy functional of 2D-AEM for CSP-ARH is

$$2\Pi_1=\boldsymbol{\chi}^{\mathrm{T}}\tilde{\boldsymbol{A}}\boldsymbol{\chi}+\boldsymbol{\chi}_{,\alpha}^{\mathrm{T}}\tilde{\boldsymbol{B}}_{\alpha\beta}\boldsymbol{\chi}_{,\beta}-2\boldsymbol{\chi}^{\mathrm{T}}\boldsymbol{F}\tag{30}$$

where

$$\begin{aligned}&\tilde{\boldsymbol{A}}=\left[\begin{array}{cc}\langle\overline{\boldsymbol{D}}_e\rangle & \langle x_3\overline{\boldsymbol{D}}_e\rangle\\ \langle x_3\overline{\boldsymbol{D}}_e\rangle & \langle x_3^2\overline{\boldsymbol{D}}_e\rangle\end{array}\right],\tilde{\boldsymbol{B}}_{\alpha\beta}=\left\langle\boldsymbol{D}_{s_{\alpha\beta}}\hat{\boldsymbol{D}}^T\hat{\boldsymbol{D}}-\boldsymbol{C}_\alpha^{*\mathrm{T}}\boldsymbol{D}_s^{-1}\boldsymbol{C}_\beta^*\right\rangle\\&\tilde{\boldsymbol{F}}=\left\langle\hat{\boldsymbol{D}}^{\mathrm{T}}f_3\right\rangle-\left\langle\boldsymbol{C}_\alpha^{*\mathrm{T}}\boldsymbol{D}_s^{-1}\tilde{\boldsymbol{f}}_{,\alpha}^*\right\rangle\end{aligned}\tag{31}$$

Considering the relationship between the strains measures $\boldsymbol{R}$ of Reissner-Mindlin plate and $\boldsymbol{\gamma}=\left[\begin{array}{cc}2\gamma_{13} & 2\gamma_{23}\end{array}\right]^{\mathrm{T}}$ as

$$\boldsymbol{\epsilon}=\boldsymbol{R}-\tilde{\boldsymbol{I}}_\alpha\boldsymbol{\gamma}_{,\alpha}\tag{32}$$

where

$$\tilde{\boldsymbol{I}}_1=\left[\begin{array}{cccccc}0&0&0&1&0&0\\0&0&0&0&1&0\end{array}\right]^{\mathrm{T}},\tilde{\boldsymbol{I}}_2=\left[\begin{array}{cccccc}0&0&0&0&1&0\\0&0&0&0&0&1\end{array}\right]^{\mathrm{T}}\tag{33}$$

Finally, Eq. (30) can be rewritten as

$$2\Pi_1 = \boldsymbol{R}^{\mathrm{T}}\tilde{\boldsymbol{A}}\boldsymbol{R} + \boldsymbol{\gamma}^{\mathrm{T}}\tilde{\boldsymbol{G}}\boldsymbol{\gamma} - 2\boldsymbol{R}^{\mathrm{T}}\tilde{\boldsymbol{F}} + U^* \tag{34}$$

where

$$U^* = \boldsymbol{R}^{\mathrm{T}}_{,\alpha}\overline{\boldsymbol{B}}_{\alpha\beta}\boldsymbol{R}_{,\beta}, \quad \overline{\boldsymbol{B}} = \tilde{\boldsymbol{B}} + \tilde{\boldsymbol{A}}\tilde{\boldsymbol{I}}_1\tilde{\boldsymbol{G}}^{-1}\tilde{\boldsymbol{I}}_1^{\mathrm{T}}\tilde{\boldsymbol{B}} \tag{35}$$

By minimizing the value of U^* towards zero, the parameter G can be determined, which allows for the application of an asymptotically accurate Reissner-Mindlin model in the analysis of CSP-ARH.

2.4. Buckling and free vibration analysis using 2D-AEM

The problem is formulated by starting with the Lagrangian of the system as

$$L = T - U \tag{36}$$

Letting $u_i(t) = C_1 e^{i\omega t}$, the element strain energy U_e and kinematical energy T_e can be expressed as [50]

$$U = \frac{1}{2}\int_{A_e} \boldsymbol{\kappa}^{\mathbf{T}}\boldsymbol{D}\boldsymbol{\kappa}\, dA_e = \frac{1}{2}\boldsymbol{\delta}^{\mathbf{T}}\boldsymbol{K}\boldsymbol{\delta} \tag{37}$$

$$T = \frac{1}{2}\rho^{(*)}\int_A \left[\left(\frac{\partial u_1}{\partial t}\right)^2 + \left(\frac{\partial u_2}{\partial t}\right)^2 + \left(\frac{\partial u_3}{\partial t}\right)^2\right] dA = \frac{1}{2}\omega^2\bar{\boldsymbol{u}}^{\mathrm{T}}\boldsymbol{M}\bar{\boldsymbol{u}} \tag{38}$$

where $\boldsymbol{M}$ and $\boldsymbol{K}$ are total mass and stiffness matrix, and ω is angular frequency.

Upon minimizing the total potential energy, Eq. (38) is obtained as

$$(\boldsymbol{K} - \omega^2\boldsymbol{M})\bar{\boldsymbol{u}} = 0 \tag{39}$$

By utilizing the material constants and reference stiffness of the face sheet, the resulting frequency can be normalized as

$$\bar{\omega} = \omega\frac{a^2}{h}\sqrt{\frac{\rho_f}{E_2}} \tag{40}$$

where $\bar{\omega}$ is the non-dimensional frequency.

Introducing the unknown multiplier λ to account for the pre-buckling condition, the buckling problem can be expressed as

$$(\boldsymbol{K} + \lambda\boldsymbol{K}_G)\boldsymbol{\delta} = 0 \tag{41}$$

The geometric stiffness matrix $\boldsymbol{K}_G$ can be expressed as

$$\boldsymbol{K}_G = h \int_A \boldsymbol{G}_i^T \boldsymbol{S} \boldsymbol{G}_j dA \tag{42}$$

where

$$\boldsymbol{G}_i = \begin{bmatrix} \frac{\partial N_i}{\partial x_1} & \frac{\partial N_i}{\partial x_2} & 0 & 0 & 0 & 0 \\ 0 & 0 & \frac{\partial N_i}{\partial x_1} & \frac{\partial N_i}{\partial x_2} & 0 & 0 \\ 0 & 0 & 0 & 0 & \frac{\partial N_i}{\partial x_1} & \frac{\partial N_i}{\partial x_2} \end{bmatrix}^{\tau} \tag{43}$$

$$\boldsymbol{S} = \begin{bmatrix} \overline{\boldsymbol{S}} & 0 & 0 \\ 0 & \overline{\boldsymbol{S}} & 0 \\ 0 & 0 & \overline{\boldsymbol{S}} \end{bmatrix}, \quad \overline{\boldsymbol{S}} = \begin{bmatrix} N_{x_1} & N_{x_1 x_2} \\ N_{x_1 x_2} & N_{x_2} \end{bmatrix} \tag{44}$$

3. Validation example

To validate the accuracy and effectiveness of 2D-AEM, a 60 mm × 38.64 mm CSP-ARH was designed, as showed in Fig. 2. The macro structure, depicted in Fig. 2(a), comprises 10 × 10 repeat subs-tructures with $h_t = h_b = 0.1h_c = 0.1$ mm, $2l_1 = l_2 = 2$ mm, $t_1 = t_2 = 0.1$ mm, and $\theta = 30°$. The facesheet is composed of T300/914 epoxy composite, while the reentrant honeycomb core is made of aluminum. The properties of the aluminum core are taken as $\nu = 0.3$, and $\rho = 2700\ \mathrm{kg \cdot m^{-3}}$. The elastic properties of the composite facesheets are [46]: $E_1 = E_2 = 10.20$ GPa, $E_3 = 5.50$ GPa, $G_{12} = 1.58$ GPa, $G_{13} = G_{23} = 1.56$ GPa, $\nu_{12} = 0.183$, $\nu_{13} = \nu_{23} = 0.512$, and the density is $\rho = 1520\,\mathrm{kg \cdot m^{-3}}$.

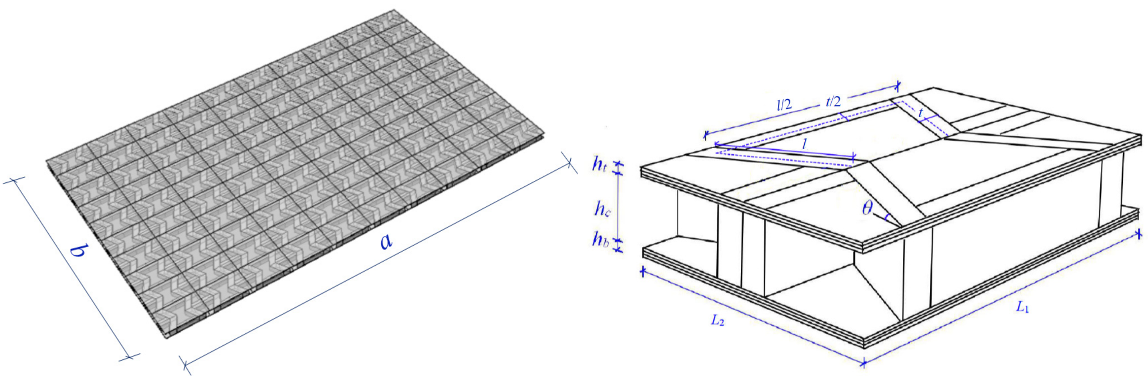

(a) Overall structure of CSP-ARH (b) Details of 3D Unit Cell

Figure 2: Structure of unit cell and CSP-ARH.

Table 1 presents the buckling loads and natural frequencies of CSP-ARH under the condition of four-sided simple support as obtained by both 2D-AEM and 3D-FEM. 3D-FEM is modeled in Abaqus using 20-noded brick elements with reduced integration (C3D20R). First four buckling and vibration modes of CSP-ARH under simple-supported boundary condition are shown in Fig. 3. Table 2 compares the first-order buckling loads and natural frequencies under different boundary conditions, and the schematic diagram of the boundary conditions is shown in Fig. 4. The short sides of the buckling analysis model are subjected to uniform uniaxial compression. The results show that the difference between the buckling loads and natural frequencies obtained from 2D-AEM and 3D-FEM is within 3%. These findings suggest that the mechanical properties of CSP-ARH, as predicted by 2D-AEM, are accurate and suitable for the subsequent structural optimization analysis. Fig. 5 displays first buckling and vibration modes of CSP-ARH under four boundary conditions.

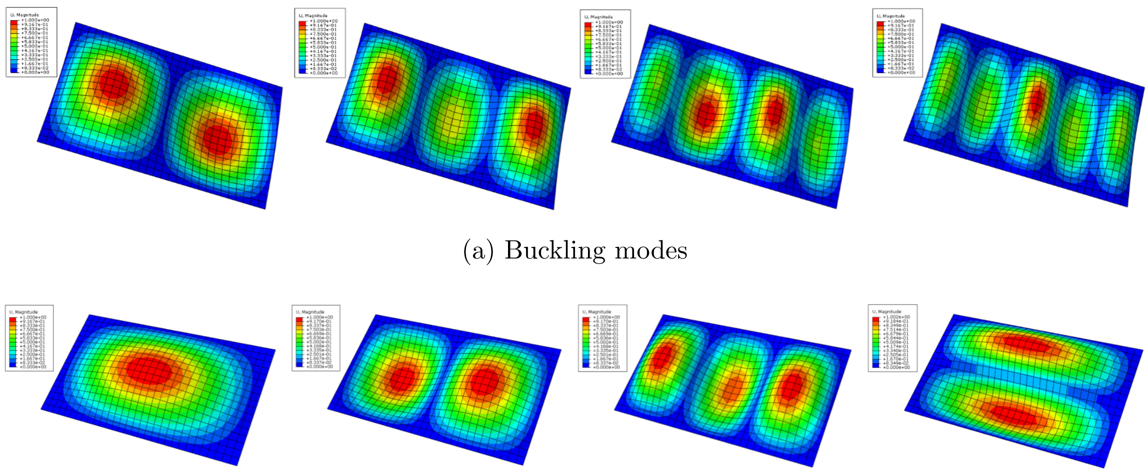

(a) Buckling modes

(b) Vibration modes

Figure 3: First four buckling and vibration modes of CSP-ARH under simple-supported boundary condition.

Table 3 compares the modeling costs and computational time between the 2D-AEM and 3D-FEM. The 2D-AEM demonstrates significant advantages in computational efficiency due to a substantial decrease in the number of modeling elements. Specifically, the 2D-AEM employs 570 shell elements compared to the 108,806 solid elements used in the 3D-FEM. As a result, the buckling analysis requires only 20 seconds, while the free vibration analysis takes approximately 12 seconds. On the other hand, the 3D-FEM

Table 1: Comparison of the buckling loads and natural frequencies of CSP-ARH under simple-supported boundary condition obtained by 2D-AEM and 3D-FEM.

Orders	Buckling loads (N)		Natural frequency (Hz)	
	2D-AEM	3D-FEM	2D-AEM	3D-FEM
1	1903.42	1906.98	332.56	337.63
2	2110.61	2123.36	476.57	496.80
3	3051.47	3079.59	769.89	784.68
4	4271.91	4315.10	845.95	862.93

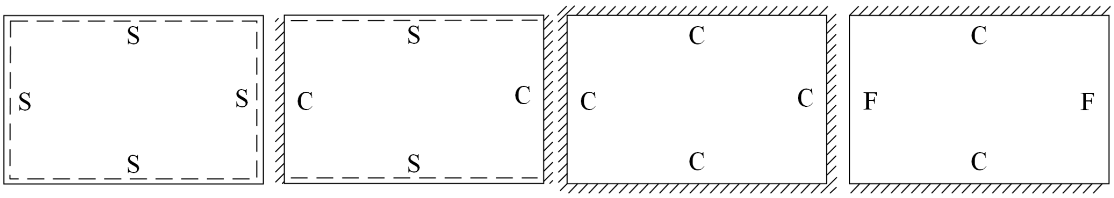

(a) SSSS (b) CCSS (c) CCCC (d) FFCC

Figure 4: Typical combinations of different boundary conditions for CSP-ARH (S: simply support, C: clamped support, F: free).

Table 2: Comparison of the first-order buckling loads and natural frequencies of CSP-ARH with four boundary conditions obtained by 2D-AEM and 3D-FEM.

Boundary conditions	Buckling loads (N)		Natural frequency (Hz)	
	2D-AEM	3D-FEM	2D-AEM	3D-FEM
SSSS	1903.42	1906.98	332.56	337.63
CCSS	2569.28	2597.471	376.52	383.71
CCCC	3005.08	2969.24	498.45	507.11
FFCC	976.75	983.88	435.23	442.48

demands considerably greater computational time, with the buckling analysis taking 31 minutes and the free vibration analysis requiring 4 minutes.

In summary, the 2D-AEM significantly reduces the workload associated with numerical analysis of CSP-ARH when compared to the 3D-FEM, while still maintaining a satisfactory level of computational accuracy. This methodology offers an accurate and efficient approach for analyzing honeycomb sandwich structures, thereby facilitating fur-

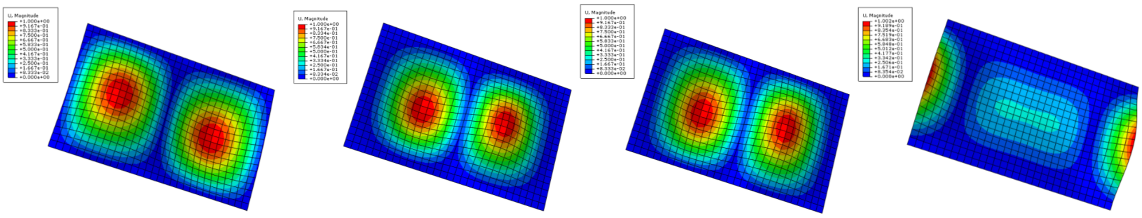

(a) Buckling modes

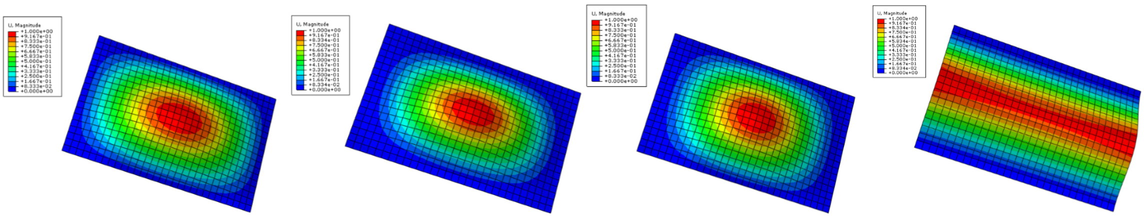

(b) Vibration modes

Figure 5: First buckling and vibration modes of CSP-ARH under different boundary conditions (From left to right: SSSS, CCSS, CCCC, FFCC).

Table 3: Modeling efficiency and time-consuming of 2D-AEM and 3D-FEM in buckling and free vibration analysis.

Items	3D-FEM	2D-AEM	
		3D unit cell	2D plate
Element type	C3D20R	C3D20R	S8R5
Number of elements	108,806	13,408	570
Number of nodes	164,339	19,746	620
Buckling	31 min	/	20 s
Free vibration	4 min	/	12 s

ther research on optimizing CSP-ARH.

4. Optimal analysis of CSP-ARH

4.1. Particle swarm optimization

The PSO algorithm is a stochastic method based on a population referred to as a swarm, with individual members called particles. Each particle is determined by two components: its position X and velocity V. In this algorithm, for an optimization problem in a search space of dimension $\hat{V}$, and with a total number of particles in the swarm as N_p, during the jth iteration, the current position and velocity of the ith particle can be represented as $\boldsymbol{X}_i(j) = \left(X_i^1(j), X_i^2(j), \cdots, X_i^V(j)\right)$ and $\boldsymbol{V}_i(j) = \left(V_i^1(j), V_i^2(j), \cdots, V_i^V(j)\right)$, respectively. The update position vector of the kth variable of a particle, $\boldsymbol{X}_i(j)$, is

$$X_i^k(j+1) = X_i^k(j) + V_i^k(j+1) \tag{45}$$

The update velocity vector $V_i(j)$ can be represented by [40]

$$\begin{aligned} &V_i^k(j+1) = w_{\text{inertia}}\, V_i^k(j) + c_1 r_i^k(j)\left(X_{i,pbst}^k(j) - X_i^k(j)\right) \\ &+c_2 R_i^k(j)\left(X_{i,gbest}^k(j) - X_i^k(j)\right) \end{aligned} \tag{46}$$

where $X_{i,pbst}^k(j)$ and $X_{i,gbest}^k(j)$ respectively represent the local and global best positions of the kth variable of the ith particle during the jth iteration; r_i and R_i are random numbers ranging from 0 to 1, c_1 and c_2 represent the learning factors; w_{inertia} is the inertia weight defined by the algorithm, which can determine the convergence rate and accuracy of the algorithm.

From Eq. (46), it is evident that increasing the value of w_{inertia} exerts a stronger influence on the particle velocity $V_i^k(j+1)$, resulting in a greater emphasis on the velocity from the previous iteration. As a consequence, particles tend to explore distant regions rather than nearby ones, leading to faster convergence at the expense of compromised precision. Conversely, when the value of w_{inertia} is smaller, particles are more effective in exploring the local space, which improves convergence accuracy but raises the risk of becoming trapped in local optima. Therefore, in this study, a linearly decreasing inertia weight strategy is employed. During the initial iterations, when the value of w_{inertia} is larger, the algorithm benefits from its fast convergence capability. As the iterations progress, the value of w_{inertia} gradually decreases, enhancing computational precision. The expression for w_{inertia} is provided as

$$w_{\text{inertia}} = w_{\text{damp}}^j \tag{47}$$

where w_{damp} is the decay coefficient of the inertia weight.

As the number of iterations increases, it is evident that the inertia weight gradually decreases over time. To provide a visual representation of the computation and iteration steps in the algorithm, please refer to Fig. 6. The PSO control parameters are taken as $N_p = 20$, $c_1 = 1.5$, $c_2 = 2.0$ and $w_{\text{damp}} = 0.9$. Table 4 studies the convergence and accuracy of the buckling analysis using this method for laminated composite square plates under uniaxial loading. By comparison with Ref. [38], this method is verified to be feasible. In addition, as the number of elements N_e increases, the optimization results are closer to the results of the reference. It is appropriate to use 20 elements for the optimization problem.

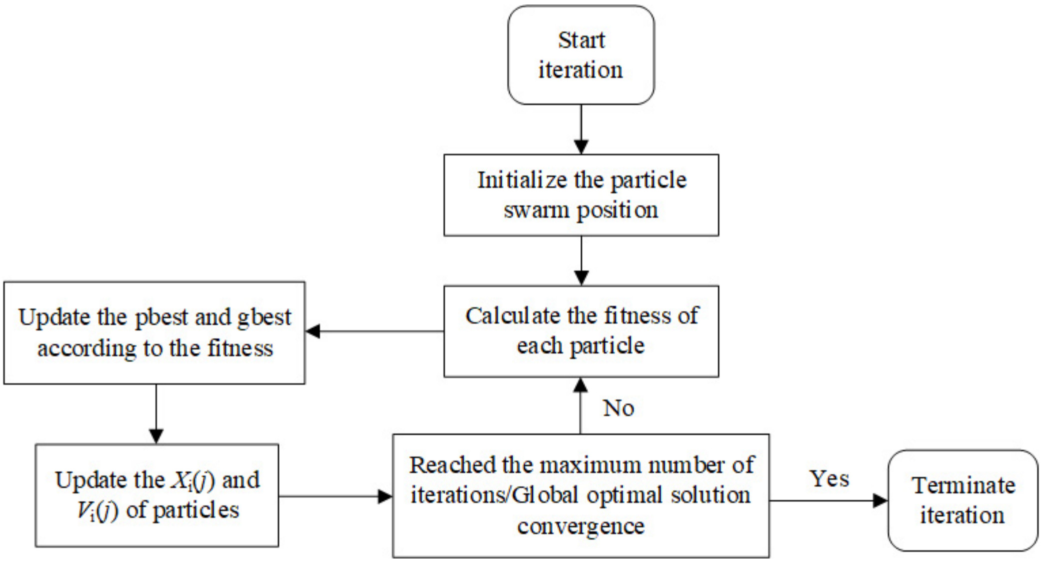

Figure 6: Pseudo-code for PSO algorithm.

Table 4: Convergence and accuracy of the non-dimensional buckling load of two layers [0°/90°] laminated composite square plates for different length to thickness ratio and boundary conditions.

N_e	a/h	Boundary conditions					
		SSFF	SSFS	SSFC	SSSS	SSSC	SSCC
10		3.915	4.301	4.932	8.781	10.771	11.532
20	5	3.910	4.292	4.924	8.769	10.761	11.506
Ref. [38]		3.907	4.288	4.917	8.764	10.757	11.501
10		4.968	5.472	6.315	11.553	17.251	21.646
20	10	4.950	4.458	6.292	11.561	17.175	21.521
Ref. [38]		4.944	5.450	6.288	11.558	17.169	21.517

4.2. Maximizing buckling load and natural frequency

Instability and vibration characteristics play a crucial role in the application of thin-walled structures. In the case of maximizing the buckling load of a simply supported sandwich panel subjected to uniformly distributed compressive loads, the panel's buckling load is obtained by solving Eq. (41), which incorporates the elastic symmetry condition of the plate. The design variables and their ranges for the PSO algorithm are specified in Table 5. These optimization problems are all defined as discrete optimization problems. For the fundamental frequency maximization problem of CSP-ARH, the same sandwich panel with simply supported boundaries is analyzed without any external force. The design variables and their ranges for the PSO algorithm remain unchanged. The structural parameters are identified as: $a = b = 700$ mm, $h_t = h_b = 0.1$ mm, $h_c = 1$ mm, $l = 2l_1 = l_2$, and $t = t_1 = t_2$. Both of these optimization problems can be expressed in the form of constrained mathematical optimization as

$$\begin{cases} \text{Find} \rightarrow x_1, x_2, x_3, x_4 \\ \text{Max.} \rightarrow P_{\text{cr}}/P_{\text{ref}} \\ \text{Subject to} \rightarrow h(x_i) \geq 0 \\ \text{Subject to} \rightarrow x_L \leq x_i \leq x_U \end{cases} \tag{48}$$

$$\begin{cases} \text{Find} \rightarrow x_1, x_2, x_3, x_4 \\ \text{Max.} \rightarrow \bar{\omega}_1/\bar{\omega}_{\text{ref}} \\ \text{Subject to} \rightarrow h(x_i) \geq 0 \\ \text{Subject to} \rightarrow x_L \leq x_i \leq x_U \end{cases} \tag{49}$$

where x_i represent design variables of CSP-ARH; x_L and x_U are the upper and lower bounds; $h_{i,j}(x) \geq 0$ is the prerequisite for forming the reentrant honeycomb cell structure; P_{cr} and $\bar{\omega}_1$ represent the critical buckling load and non-dimensional fundamental frequency of CSP-ARH; P_{ref} and $\bar{\omega}_{\text{ref}}$ are the reference value, which are taken from the regular hexagonal honeycomb composite sandwich panel with $t = 0.2$ mm, $l = 20$ mm, $\theta = 30°$, and ply mode of $[0°/90°/0°/90°]$.

Table 5: Design variables for the optimization problem of CSP-ARH.

Variables	Lower boundary	Upper boundary	Discrete intervals	Number
t(mm)	0.1	0.4	0.1	4
θ(°)	15	60	15	4
l(mm)	10	40	10	4
θ_i(°)	-90	90	15	13

Fig. 7 depicts the 1/4 structure of the honeycomb core cell. Notably, the abscissa of point A must be greater than or equal to the abscissa of point B to ensure the correct formation of the CSP-ARH, which consists of re-entrant honeycomb cells that are continuously repeated and distributed. Thus, the constraint condition can be succinctly expressed as

$$h_{i,j}(x) = \frac{l}{2} - \frac{\sin\theta l}{2} - \frac{2t}{\cos\theta} \tag{50}$$

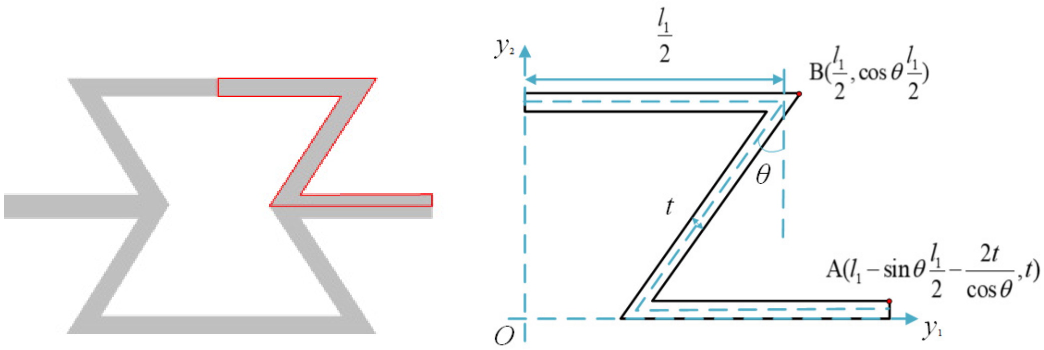

(a) Unit cell structure (b) 1/4 unit cell

Figure 7: Honeycomb core unit cell of CRHSP.

The sensitivity analysis comparison of different optimization parameters of CSP-ARH is shown in Table 6. Except for the variation parameters selected for analysis, the other parameters remain consistent with the dimensions of the reference object. In addition, since the outermost ply has the greatest impact on the mechanical properties of the sandwich panel structure among all plies, the sensitivity coefficient of the angle θ_1 of the outermost ply of the laminate is also calculated. From this table, it is obvious that t has the greatest effect on the buckling load and natural frequency of CSP-ARH, while θ_1 has the smallest impact.

The maximum iteration step $It_{\max} = 20$ was determined as the stop criteria after debugging. Each optimization problem was ultimately run for 20 iterations. Fig. 8(a) illustrates the trend of $P_{\text{cr}}/P_{\text{ref}}$ during the buckling load optimization process. It can be observed that this ratio gradually increases with the number of iterations, until it stabilizes after the 10th iteration. The overall curve demonstrates an increase from 1.4415 in the initial step to 1.7840 in the final step, indicating a growth of 23.76%. Notably, the convergence of the core structure parameters, including the wall length l, wall thickness t, and cell wall inclination angle θ, occurs at the 5th iteration, followed by the convergence

Table 6: Sensitivity analysis of the optimization parameters of of CSP-ARH.

Variables	Variable change range	Fitness change range		Sensitivity coefficient	
	Δx_i	$\lvert\Delta P_{\mathrm{cr}}\rvert / P_{\mathrm{ref}}$	$\lvert\Delta\bar{\omega}_1\rvert / \bar{\omega}_{\mathrm{ref}}$	$\lvert\Delta P_{\mathrm{cr}}\rvert / P_{\mathrm{ref}}\Delta x_i$	$\lvert\Delta\bar{\omega}_1\rvert / \bar{\omega}_{\mathrm{ref}}\Delta x_i$
t	0.1	8.08E-02	3.90E-01	8.08E-01	3.90E+00
θ	15	3.58E-02	6.74E-02	2.39E-03	4.49E-03
l	10	8.11E-02	2.17E-01	8.11E-03	2.17E-02
θ_1	90	3.27E-03	8.01E-02	3.64E-05	8.90E-04

of the angles θ_i for each layer in the face layer laying method, which is achieved by the 10th iteration.

Similarly, as shown in Fig. 8(b), $\bar{\omega}_1/\bar{\omega}_{\mathrm{ref}}$ also exhibits a gradual increase with the number of iterations, ranging from 1.1340 in the initial step to 1.2075 in the final step, denoting a growth of 6.48%. The iteration curve begins to converge at the 11th step when the laying method is determined, while the core structural parameters are determined at the 4th step. For a comprehensive summary of the optimal structural parameters and the corresponding improvements, please refer to Table 7.

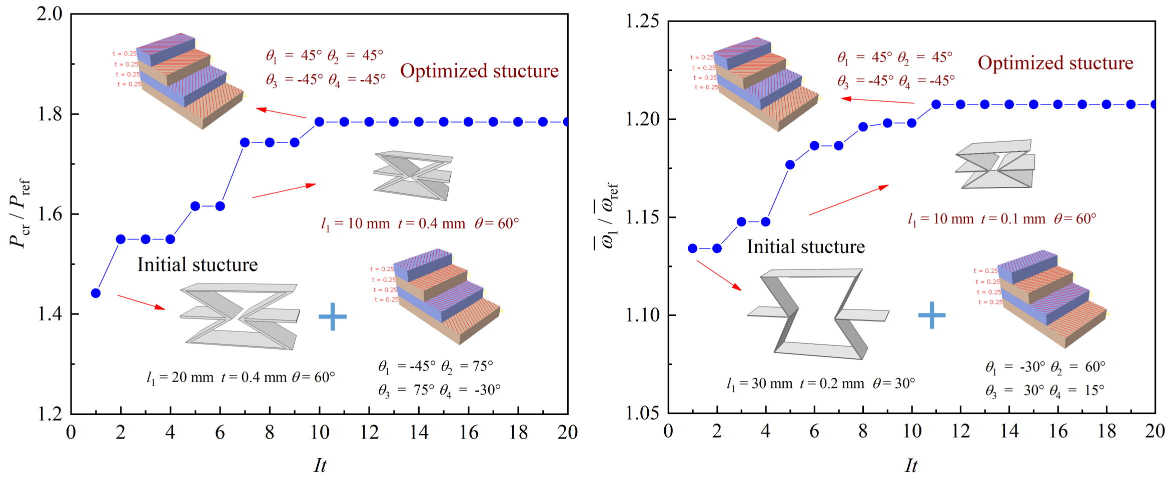

(a) $P_{\mathrm{cr}}/P_{\mathrm{ref}}$ (b) $\bar{\omega}_1/\bar{\omega}_{\mathrm{ref}}$

Figure 8: Optimization iterative curves for structural parameters of CSP-ARH.

On the basis of other conditions remaining unchanged, Table 8 and Table 9 compare the optimal structural parameters of CSP-ARH with different a/b and a/h respectively, and list their improvement amplitudes. It can be seen from the tables that as a/b and a/h change, the optimal laminate structure is basically the same, but some parameters

Table 7: The optimal structural parameters and final optimization improvement of CSP-ARH.

Max	Optimum core structure $(l/a, t/h_c, \theta/°)$	Optimum lay-up $(\theta_i/°)$	Improvement (%)
P_{cr}	[1/70, 2/75, 60]	[45/45/-45/-45]	23.76
$\bar{\omega}_1$	[1/70, 1/150, 60]	[45/45/-45/-45]	6.48

in the optimal core structure will change accordingly. The above results demonstrate the applicability and robustness of this approach.

Table 8: The optimal structural parameters and final optimization improvement of CSP-ARH with different a/b.

a/b	Optimum core structure		Optimum lay-up		Improvement	
	P_{cr}	$\bar{\omega}_1$	P_{cr}	$\bar{\omega}_1$	P_{cr}	$\bar{\omega}_1$
1	[1/70, 2/75, 60]	[1/70, 1/150, 60]	[45/45/-45/-45]	[45/45/-45/-45]	23.76	6.48
2	[1/70, 3/150, 60]	[1/70, 1/150, 45]	[-45/45/45/-45]	[-45/45/45/-45]	30.28	8.63
4	[1/70, 3/150, 60]	[1/70, 1/150, 60]	[-45/45/45/-45]	[-45/45/45/-45]	27.84	7.21

Table 9: The optimal structural parameters and final optimization improvement of CSP-ARH with different a/h $(a/b = 1)$.

a/h	Optimum core structure		Optimum lay-up		Improvement	
	P_{cr}	$\bar{\omega}_1$	P_{cr}	$\bar{\omega}_1$	P_{cr}	$\bar{\omega}_1$
700/19	[1/70, 2/75, 60]	[1/70, 1/150, 60]	[45/45/-45/-45]	[45/45/-45/-45]	23.76	6.48
1400/19	[1/70, 2/75, 45]	[1/35, 1/150, 30]	[-45/45/45/-45]	[-45/45/45/-45]	29.34	9.80
2800/19	[1/70, 2/75, 45]	[1/35, 1/150, 30]	[-45/45/45/-45]	[-45/45/45/-45]	26.15	7.92

4.2.1. Minimizing mass

To satisfy the requirement for lightweight structures, the PSO algorithm's objective function is modified to consider the mass of CSP-ARH, while keeping the core structural parameters constant. Introducing a new variable, the number of layers n_p, with each layer having a thickness of 0.5 mm. Furthermore, the constraint function incorporates a bivariate function comprising the fundamental frequency and buckling load. The optimization problem can be expressed as

$$\begin{cases} \text{Find} \rightarrow x_1, x_2, x_3, x_4 \\ \text{Min.} \rightarrow \text{mass} \\ \text{Subject to} \rightarrow h(x_i) \geq 0 \\ \text{Subject to} \rightarrow \left(\dfrac{P_{\text{cr}}}{P_{\text{ref}}} + \dfrac{\bar{\omega}_1}{\bar{\omega}_{\text{ref}}}\right)/2 \geq 1 \\ \text{Subject to} \rightarrow x_L \leq x_i \leq x_U \end{cases} \tag{51}$$

Table 10: Optimized structural parameters and weights of CSP-ARH for different ply number.

n_p	Core $(l/a, t/h_c, \theta/^\circ)$	Lay-up $(\theta_i/^\circ)$	Fitness	m (kg)
1	[1/70, 2/75, 60]	[-45]	0.6336	/
2	[1/70, 2/75, 60]	[-45/-45]	0.7245	/
3	[1/70, 2/75, 60]	[45/-45/-45]	0.8793	/
4	[2/70, 2/75, 60]	[45/45/-45/-45]	1.0377	5.8808
5	[3/70, 1/50, 60]	[45/45/45/-45/-45]	1.0203	5.0892
6	[2/35, 1/75, 60]	[45/45/45/45/-45/-45]	1.0182	4.7330

Table 10 presents the optimization outcomes for the constrained minimization problems of CSP-ARH with different numbers of layers, in which the fitness is employed to quantify the suitability of a given solution to the problem objectives. A noteworthy observation is that the maximum fitness values for sandwich structures with fewer than four layers are all below 1, indicating their inability to meet the specified constraints. Hence, these structures are not taken into consideration.

Moreover, the table highlights that an increase in the arm length l and wall thickness t leads to a decrease in the weight of the sandwich structure. Remarkably, as the number of plies, n_p, increases from 4 to 6, the weight of the sandwich structure reduces by 19.52%. However, it is worth noting that the core structural parameters for the sandwich structure with $n_p = 6$ approach the boundary of the specified range. This suggests that further increasing the number of layers would only result in a higher weight for the sandwich structure. Consequently, it can be concluded that CSP-ARH with $n_p = 6$ represents the lightest structure that satisfies the prescribed constraints. The comparison of the core layer structure when $n_p = 1$ and the optimized core layer structure when $n_p = 6$ is shown in Fig. 9.

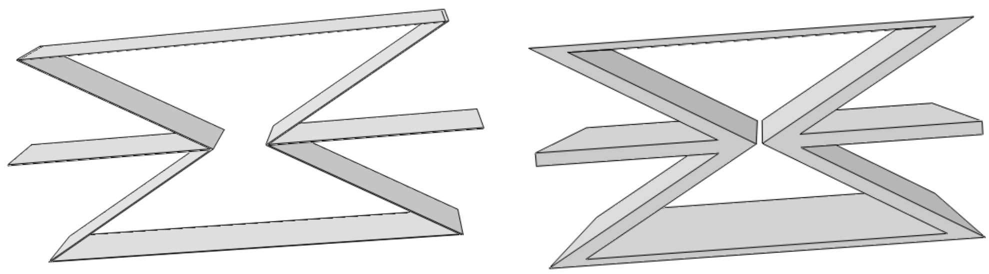

(a) $n_p = 1$

(b) $n_p = 6$

Figure 9: Initial and optimized core unit cell structures in mass optimization problem of CSP-ARH.

5. Optimal analysis of CSP-ARH-CLF

Based on the previous optimization analysis results of the buckling load and fundamental frequency for CSP-ARH incorporating straight fiber facesheets, further optimization will be conducted on the CSP-ARH-CLF based on the 2D-AEM. The influence of varying stiffness of the face layers on the buckling load and natural frequency of the sandwich panel will be discussed. The PSO optimization parameters remain unaltered, while the design variables undergo a transition from the uniform layup angles for each layer to the coefficients associated with the curved fibers' shape.

5.1. Expression of curved fiber shape

The shape of the curved fibers, as described by [50], is defined using a cubic polynomial function $f(x, y)$. The cubic polynomial function $f(x, y)$ can be expressed as

$$\begin{aligned} f(x,y) = c_{00} + c_{10}x + c_{01}y + c_{20}x^2 + c_{11}xy + c_{02}y^2 \\ +c_{30}x^3 + c_{21}x^2y + c_{12}xy^2 + c_{03}y^3 \end{aligned} \tag{52}$$

where c_{ij} ($i, j = 0, 1, 2, 3$) are the shape coefficients that determine the shape of the cubic polynomial function.

The present description is more effective and flexible than using the spline function [51] since there is no requirement for solving simultaneous equations to determine the fiber shapes and it simply accepts multi-valued functions. Ref. [50] further demonstrated the feasibility of using a cubic polynomial function to improve the natural frequency of sandwich composite with curvilinear fibers. It provides the necessary adaptability to accommodate various curve shape changes while keeping the computational load controllable. Fig. 10 illustrates the 3D surface and presents the projected 2D contour lines of the surface on the xoy horizontal plane. By modifying the coefficients c_{ij}, the expression in Eq. (52) can be employed to depict the shape of a sequence of 2D curves.

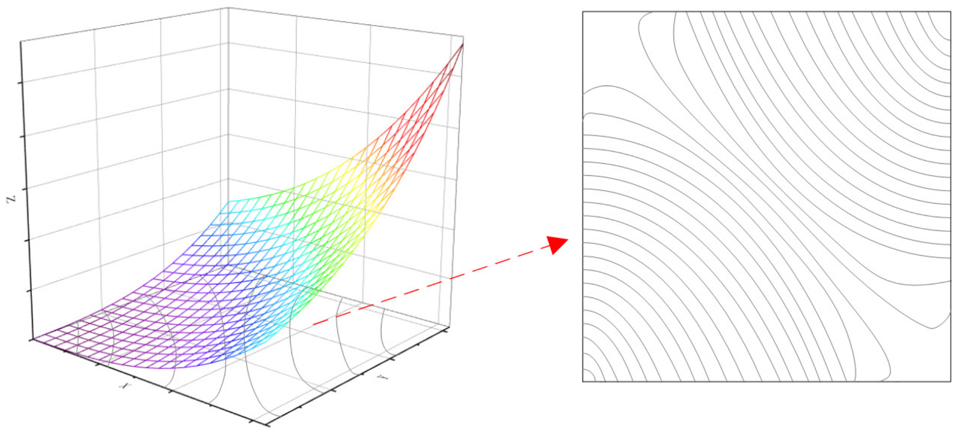

Figure 10: Curve fiber diagram defined by cubic polynomial function $f(x, y)$.

Representing curved fibers with continuous bending in finite element analysis is often challenging. Typically, a discretization approach is employed, treating the fibers as short straight segments within each element [52]. In this study, a 20 × 20 grid consisting of discrete elements is utilized to depict curved fibers arranged from left to right and bottom to top. The fiber orientation angle $\theta_{n,q}$ at the nth row and qth column of an element is defined as the tangent direction of the 2D contour line. This angle can be determined by calculating the tangent using the coordinates (x_c, y_c) of the element center as

$$\theta_{n,q}\left(x_c, y_c\right) = \tan^{-1}\left(-\frac{\partial f/\partial x}{\partial f/\partial y}\right)\bigg|_{x=x_c, y=y_c} \tag{53}$$

5.2. Optimization steps for curved fiber facesheets

To enhance computational efficiency and minimize the number of iterations in the optimization analysis, we combined the layerwise optimization approach (LOA) with the optimization of curved fiber layers, as proposed by Narita et al. [53]. Building upon the optimal solution obtained for the straight fiber layers in the previous section, the layerwise optimization process is depicted in Fig. 11. Initially, we assumed a ply mode of [45°/45°/-45°/-45°], which corresponds to the optimal ply mode for maximum buckling load and natural frequency of the straight fibers, while keeping other structural and material parameters constant.

In Step 1 of the process, we modified the shape coefficients of the cubic polynomial function $f(x, y)$ and searched for the optimal orientation angle for the first layer of curved fibers. Subsequently, we replaced the angle of the straight fibers with this optimal angle. Moving to Step 2, we searched for the optimal angle for the second layer of curved fibers while keeping the angle of the first layer fixed. This process continues iteratively until all layer angles are determined in Step 4, representing the termination of the optimization process.

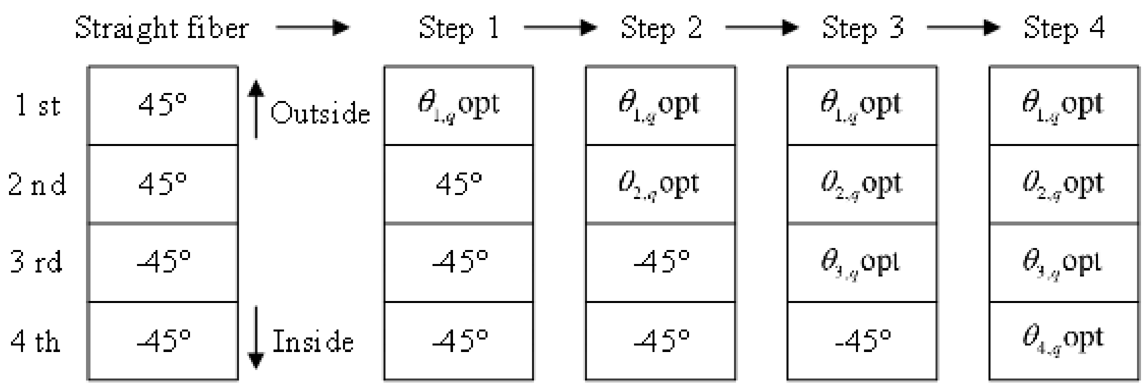

Figure 11: Laminate structure optimization problem of curved fiber facesheet.

5.3. *Expression of curved fiber shape*

In many cases, the boundaries of sandwich panels remain straight as a consequence of external structural constraints and the in-plane bending stiffness of the panel, as stated by Vescovini et al. [54]. Fig. 12 presents the loading conditions and the pre-buckling deformation mode of the sandwich panel. This pre-buckling mode confines the redistribution of load along the boundary, leading to non-uniform face stresses when a displacement is introduced along the x_1 direction, as depicted in Fig. 12(b).

In the pre-buckling analysis, the transverse boundary of the sandwich panel experiences uniform end shortening. As a result, the boundary conditions can be defined as

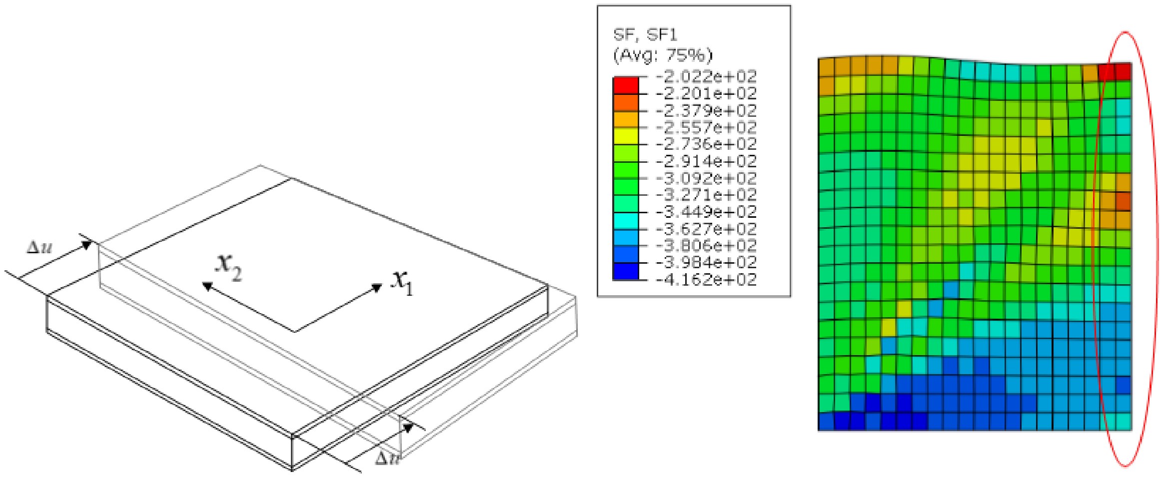

(a) Deformation shape of sandwich panel (b) Boundary force of sandwich panel

Figure 12: Undeformed and deformed configurations in the prebuckled state.

$$
\begin{aligned}
&u(x_1 = a/2) = -\Delta_u \\
&u(x_1 = -a/2) = 0
\end{aligned}
\tag{54}
$$

The average value of the axial force per unit length supported by the sandwich panel can be represented as

$$
N_{x_1,avg} = \frac{1}{b}\int_{-b/2}^{b/2} N_{x_1}(x_2)\mathrm{d}y \tag{55}
$$

where $N_{x_1,avg}$ represents the average surface force distributed along the x_2 direction at the boundary, which is carried by the sandwich panel.

The buckling load under a unit displacement load, unlike the buckling load calculated under a uniform load in previous studies, aligns more closely with the aforementioned scenario. This value can be utilized in solving for the critical buckling load P_{cr} as

$$
P_{cr} = \lambda N_{x_1,avg} \tag{56}
$$

The free vibration analysis of CSP-ARH-CLF employs the same methodology as CSP-ARH. The optimization problem for the critical buckling load and fundamental frequency of CSP-ARH-CLF can be formulated as

$$
\begin{cases}
\text{Find} \rightarrow c_{ij}^{(k)}(i,j = 0,1,2,3; k = 1,2,3,4) \\
\text{Max.} \rightarrow P_{\mathrm{cr}}/P_{\mathrm{opt}} \quad \text{and} \quad \bar{\omega}_1/\bar{\omega}_{\mathrm{opt}}
\end{cases}
\tag{57}
$$

where P_{opt} and $\bar{\omega}_{opt}$ denote the optimal critical buckling load and non-dimensional fundamental frequency of CSP-ARH, $c_{ij}^{(k)}$ is the coefficients of the kth layer in Eq. (53), and their incremental changes are set to 1. It has been determined that the influence of decimal values on the angle of a single element is negligible and can be disregarded.

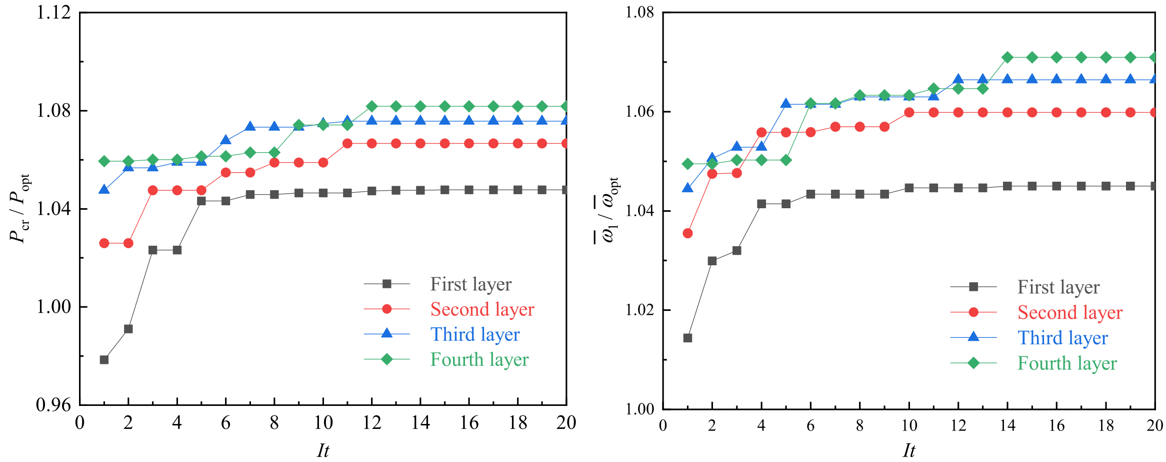

(a) $P_{\mathrm{cr}}/P_{\mathrm{opt}}$ (b) $\bar{\omega}_1/\bar{\omega}_{\mathrm{opt}}$

Figure 13: Maximization iterative curves for curved fiber facesheets in CSP-ARH-CLF.

Fig. 13 illustrates the gradual increase in the fitness of the function throughout the optimization process of CSP-ARH-CLF. Across the first to fourth layers, the fitness of the buckling load improved by 4.77%, 6.67%, 7.57%, and 8.18% respectively compared to the optimal solution of CSP-ARH. Similarly, the fitness of the fundamental frequency improved by 4.05%, 5.98%, 6.64%, and 7.09% respectively compared to the optimal solution of CSP-ARH. These results indicate that the outermost laminate pair has a greater impact and provides greater optimization improvement with decreasing layer number. This is demonstrated in the figure by the gradual reduction in the difference between the maximum fitness of the current layer after iteration and that of the previous layer as the layer number increases. The entire optimization analysis consisted of 80 iterations, where each iteration included 20 sets of shape coefficients. The buckling load increased by 8.18% compared to that of CSP-ARH, while the fundamental frequency of the curved fiber board ultimately improved by 7.09% compared to that of CSP-ARH.

The optimized layer layouts obtained through the hierarchical optimization method are depicted in Fig. 14. The figure illustrates substantial alterations in the unit angles of the curved fiber facesheets as compared to the previous straight fiber facesheets. Notably, as the distance from the diagonal increases, the unit angles experience more pronounced changes. However, the unit angles along the diagonal remain in close proximity to the

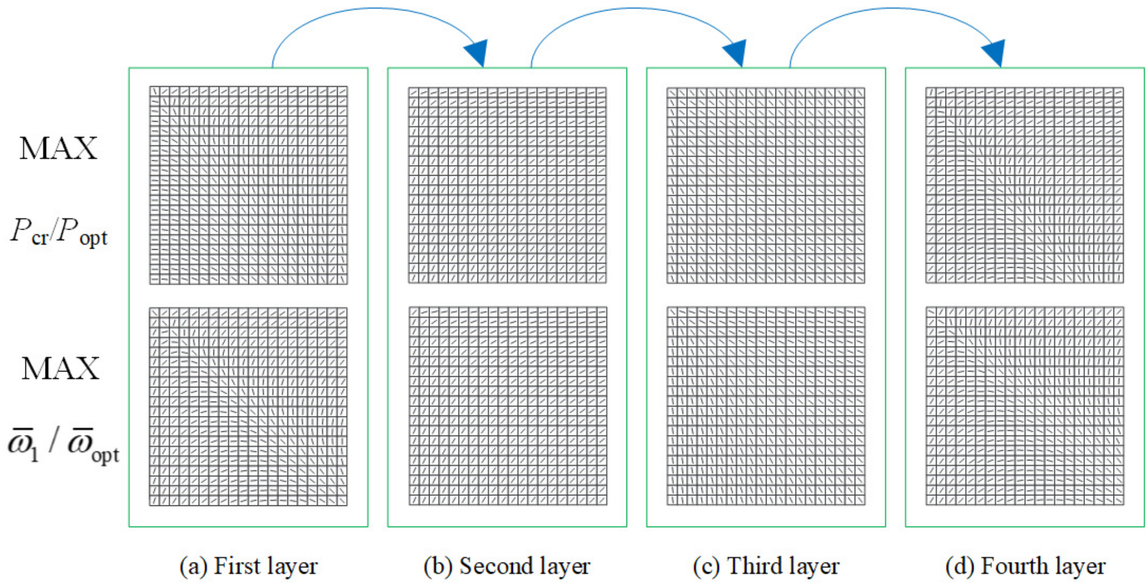

Figure 14: Laminate structures with optimum curvilinear fiber shapes in CSP-ARH-CLF after maximizing fitness.

optimal layup angle of 45° for the straight fiber facesheets, thereby validating the accuracy of the previous iteration results.

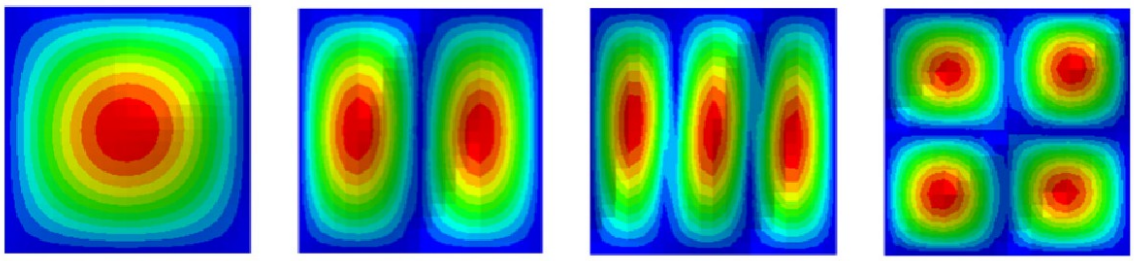

(a) CSP-ARH

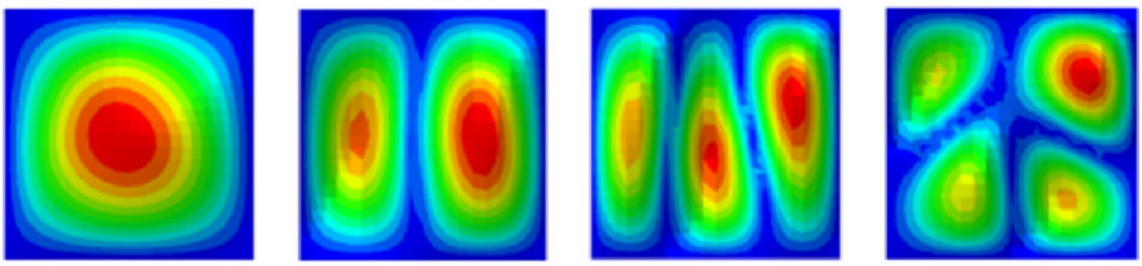

(b) CSP-ARH-CLF

Figure 15: First four buckling modes for CSP-ARH and CSP-ARH-CLF with optimum solution.

Fig. 15 depicts the first four buckling modes of CSP-ARH and CSP-ARH-CLF after optimization. The findings reveal a transition in the buckling modes of the plate from a half-wave shape to four half-wave shapes as the mode order increases. While the first four buckling modes of CSP-ARH-CLF demonstrate slight variations compared to those of CSP-ARH, they remain consistent overall. Fig. 16 presents the optimized vibration modes of CSP-ARH for the first four modes. The results illustrate that with increasing mode order, the vibration modes of the plate progress from a half-wave shape to four half-wave shapes, with the waveform distributed in a reverse pattern alongside the diagonal of the plate. With the exception of the first mode, the vibration modes of CSP-ARH-CLF differ significantly from those of CSP-ARH.

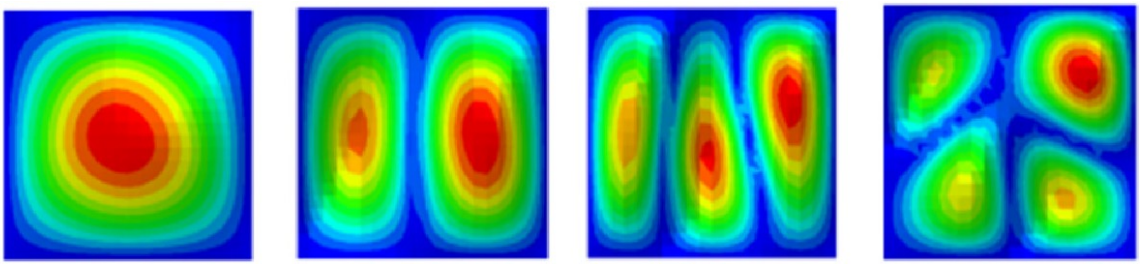

(a) CSP-ARH

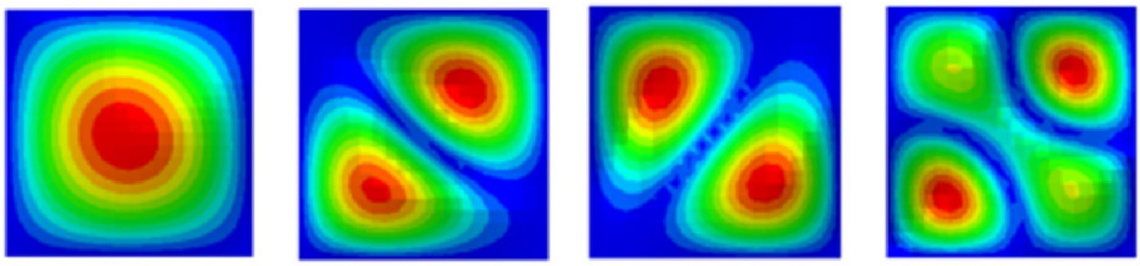

(b) CSP-ARH-CLF

Figure 16: First four vibration modes for CSP-ARH and CSP-ARH-CLF with optimum solution.

6. Conclusions

The present study proposes a framework for optimizing the buckling load and vibration frequency of CSP-ARH utilizing the homogenized equivalent model (2D-AEM) and the PSO algorithm. That is, a PSO algorithm with constraints based on the unit cell structure is integrated to optimize the buckling load, vibration frequency, and mass of

CSP-ARH or CSP-ARH-CLF. The optimization parameters include the ply mode of the CFRP surface layer and the structural parameters of the core layer. These capabilities have been utilized to yield several results, which provide some valuable references for the application of the NPR honeycomb sandwich structures. The conclusions can be drawn:

(1) The comparative results demonstrate that the VAM-based 2D-AEM is capable of efficiently and accurately predicting the buckling and vibration behaviors of CSP-ARH. The integration of shape constraints in the PSO algorithm enhances the efficiency of global search. Consequently, it becomes feasible to obtain optimal parameters for fabricating sandwich panels with desirable mechanical properties.

(2) During the buckling analysis of CSP-ARH with $a = b$, it is evident that the buckling load escalates as the wall length (l) decrease, as well as the wall thickness (t) and the cell angle (θ) increase. In contrast, in the free vibration analysis, the natural frequency rises when the wall length (l) and the inclination angle of the cell wall (θ) are larger, as well as the wall thickness (t) is thinner.

(3) Within a specific range of structural parameter variations in CSP-ARH, the fitness of the buckling load experiences a notable increase from 1.4415 to 1.7840, indicating a substantial growth of 23.76%. Likewise, the fitness of the fundamental frequency demonstrates an increase from 1.1340 to 1.2075, resulting in a growth of 6.48%. These outcomes imply that the alterations in the structural parameters of CSP-ARH exert a more significant influence on its buckling behavior when compared to its vibration behavior.

(4) The optimized version of CSP-ARH-CFL demonstrates significant enhancements of 8.18% and 7.09% in the buckling load and natural frequency, respectively, compared to the optimal solution achieved for CSP-ARH. It is worth mentioning that the ply angle of discrete units along the diagonal remains closely aligned with the optimal ply angle of 45° for straight fiber laminate in CSP-ARH. However, as the discrete units move away from the diagonal of the sandwich panel, their angle variations become more pronounced.

Acknowledgements

The work is sponsored by the National Natural Science Foundation of China (Grant Numbers: 51968046).

[1] He M, Hu W. A study on composite honeycomb sandwich panel structure. Mater Design, 2008, 29(3): 709-713.

[2] Usta F, Türkmen H S, Scarpa F. Low-velocity impact resistance of composite sandwich panels with various types of auxetic and non-auxetic core structures. Thin Wall Struct, 2021, 163: 107738.

[3] Kaman M O, Solmaz M Y, Turan K. Experimental and numerical analysis of critical buckling load of honeycomb sandwich panels. J Compos Mater, 2010, 44(24): 2819-2831.

[4] Sun G, Huo X, Chen D, et al. Experimental and numerical study on honeycomb sandwich panels under bending and in-panel compression. Mater Design, 2017, 133: 154-168.

[5] Abbadi A, Koutsawa Y, Carmasol A, et al. Experimental and numerical characterization of honeycomb sandwich composite panels. Simul Model Pract Th, 2009, 17(10): 1533-1547.

[6] Catapano A, Montemurro M. A multi-scale approach for the optimum design of sandwich plates with honeycomb core. Part I: homogenisation of core properties. Compos Struct, 2014, 118: 664-676.

[7] Choi J B, Lakes R S. Non-linear properties of metallic cellular materials with a negative Poisson's ratio. J Mater Sci, 1992, 27(19): 5375-5381.

[8] Choi J B, Lakes R S. Fracture toughness of re-entrant foam materials with a negative Poisson's ratio: experiment and analysis. Int J Fracture, 1996, 80(1): 73-83.

[9] Ingrole A, Hao A, Liang R. Design and modeling of auxetic and hybrid honeycomb structures for in-plane property enhancement. Mater Design, 2017, 117: 72-83.

[10] Frostig Y, Baruch M, Vilnay O, et al. High-order theory for sandwich-beam behavior with transversely flexible core. J Eng Mech, 1992, 118(5): 1026-1043.

[11] Phan C N, Frostig Y, Kardomateas G A. Analysis of sandwich beams with a compliant core and with in-plane rigidity-extended high-order sandwich panel theory versus elasticity. Int J Appl Mech, 2012;79(4):041001.

[12] Phan C N, Kardomateas G A, Frostig Y. Global buckling of sandwich beams based on the extended high-order theory. AIAA J, 2012, 50(8): 1707-1716.

[13] Phan C N, Bailey N W, Kardomateas G A, et al. Wrinkling of sandwich wide panels/beams based on the extended high-order sandwich panel theory: formulation, comparison with elasticity and experiments. Arch Appl Mech, 2012, 82: 1585-1599.

[14] Shi G, Tong P. Local buckling of honeycomb sandwich plates under action of transverse shear forces. AIAA J, 1994, 32(7):1520-1524.

[15] Rais-Rohani M, Marcellier P. Buckling and vibration analysis of composite sandwich plates with elastic rotational edge restraints. AIAA J, 1999, 37(5): 579-587.

[16] Nayak A K, Moy S S J, Shenoi R A. A higher order finite element theory for buckling and vibration analysis of initially stressed composite sandwich plates. J Sound Vib, 2005, 286(4-5): 763-780.

[17] Liu J, Cheng Y S, Li R F, et al. A semi-analytical method for bending, buckling, and free vibration analyses of sandwich panels with square-honeycomb cores. Int J Struct Stab Dy, 2010, 10(01): 127-151.

[18] Wang Y, Zhang Z, Xue X, et al. Free vibration analysis of composite sandwich panels with hierarchical honeycomb sandwich core. Thin Wall Struct, 2019, 145: 106425.

[19] Xiao P, Yifeng Z, Jie S, et al. Global buckling analysis of composite honeycomb sandwich plate with negative Poisson's ratio (CHSP-NPR) using variational asymptotic equivalent model. Compos Struct, 2021, 264: 113721.

[20] Quang V D, Quan T Q, Tran P. Static buckling analysis and geometrical optimization of magneto-electro-elastic sandwich plate with auxetic honeycomb core. Thin Wall Struct, 2022, 173: 108935.

[21] Sarafraz M, Seidi H, Kakavand F, et al. Free vibration and buckling analyses of a rectangular sandwich plate with an auxetic honeycomb core and laminated three-phase polymer/GNP/fiber face sheets. Thin Wall Struct, 2023, 183: 110331.

[22] Scarpa F, Tomlinson G. Theoretical characteristics of the vibration of sandwich plates with in-plane negative Poisson's ratio values. J Sound Vib, 2000, 230(1): 45-67.

[23] Zhu X, Zhang J, Zhang W, et al. Vibration frequencies and energies of an auxetic honeycomb sandwich plate. Mech Adv Mater Struc, 2019, 26(23): 1951-1957.

[24] Singh S J, Harsha S P. Free vibration analysis of sandwich plate with honeycomb core and FGM face sheets[M]//Advances in Systems Engineering: Select Proceedings of NSC 2019. Singapore: Springer Singapore, 2021: 905-917.

[25] Zhu S, Li J, Qiao Z, et al. Multiple Periodic Vibrations of Auxetic Honeycomb Sandwich Plate with 1: 2 Internal Resonance. J Nonlinear Math Phy, 2022, 29(2): 423-444.

[26] Diniz C A, Cunha S S, Gomes G F, et al. Optimization of the layers of composite materials from neural networks with TsaiCWu failure criterion. J Fail Anal Prev, 2019, 19: 709-715.

[27] Francisco M B, Junqueira D M, Oliver G A, et al. Design optimizations of carbon fibre reinforced polymer isogrid lower limb prosthesis using particle swarm optimization and Lichtenberg algorithm. Eng Optimiz, 2021, 53(11): 1922-1945.

[28] Pereira J L J, Francisco M B, Ribeiro R F, et al. Deep multiobjective design optimization of CFRP isogrid tubes using lichtenberg algorithm. Soft Comput, 2022, 26(15): 7195-7209.

[29] Guedes H C, Pereira J L J, Gomes G F. Multi-objective parametric optimization of a composite high-performance prostheses using metaheuristic algorithms. Struct Multidiscip O, 2023, 66(8): 189.

[30] Kennedy J, Eberhart R. Particle swarm optimization[C]//Proceedings of ICNN'95-international conference on neural networks. IEEE, 1995, 4: 1942-1948.

[31] Marini F, Walczak B. Particle swarm optimization (PSO), A tutorial. Chemometr Intell Lab, 2015, 149: 153-165.

[32] Cho H K. Maximizing structure performances of a sandwich panel with hybrid composite skins using particle swarm optimization algorithm. J Mech Sci Technol, 2009, 23(12): 3143-3152.

[33] Mohammadian M, Fereidoon A. Multi objective optimization of sandwich panels using particle swarm algorithm. Modares Mechanical Engineering, 2015, 14(1): 72-82.

[34] Gholami M, Alashti R A, Fathi A. Optimal design of a honeycomb core composite sandwich panel using evolutionary optimization algorithms. Compos Struct, 2016, 139: 254-262.

[35] Wang Y, Zhao W, Zhou G, et al. Analysis and parametric optimization of a novel sandwich panel with double-V auxetic structure core under air blast loading. Int J Mech Sci, 2018, 142: 245-254.

[36] Feng J, Fu J, Shang C, et al. Sandwich panel design and performance optimization based on triply periodic minimal surfaces. Comput Aided Design, 2019, 115: 307-322.

[37] Vosoughi A R, Darabi A, Anjabin N, et al. A mixed finite element and improved genetic algorithm method for maximizing buckling load of stiffened laminated composite plates. Aerosp Sci Technol, 2017, 70: 378-387.

[38] Vosoughi A R, Darabi A, Forkhorji H D. Optimum stacking sequences of thick laminated composite plates for maximizing buckling load using FE-GAs-PSO. Compos Struct, 2017, 159: 361-367.

[39] Namvar A R, Vosoughi A R. Design optimization of moderately thick hexagonal honeycomb sandwich plate with modified multi-objective particle swarm optimization by genetic algorithm (MOPSOGA). Compos Struct, 2020, 252: 112626.

[40] Moradi S, Vosoughi A R, Anjabin N. Maximum buckling load of stiffened laminated composite panel by an improved hybrid PSO-GA optimization technique. Thin Wall Struct, 2021, 160: 107382.

[41] Cesnik C E S, Hodges D H. VABS: a new concept for composite rotor blade cross-sectional modeling. J Am Helicopter Soc, 1997, 42(1): 27-38.

[42] Yu W, Hodges D H, Volovoi V, et al. On Timoshenko-like modeling of initially curved and twisted composite beams. Int J Solids Struct, 2002, 39(19): 5101-5121.

[43] Yu W, Volovoi V V, Hodges D H, et al. Validation of the variational asymptotic beam sectional analysis. AIAA J, 2002, 40(10): 2105-2112.

[44] Yifeng Z, Lei C, Yu W. Variational asymptotic modeling of the thermomechanical behavior of composite cylindrical shells. Compos Struct, 2012, 94(3): 1023-1031.

[45] Xiao P, Yifeng Z, Dan L, et al. Accurate recovery of 3D local field in FRP laminated beam based on asymptotic dimension reduction model. Constr Build Mater, 2019, 207: 357-372.

[46] Xiao P, Yifeng Z, Zheng S, et al. Estimation of effective properties of composite sandwich panels with negative Poisson's ratio by using variational asymptotic multiscale method. Mater Today Commun, 2020, 23: 101072.

[47] Peng X, Zhong Y, Shi J, et al. Free flexural vibration analysis of composite sandwich plate with reentrant honeycomb cores using homogenized plate model. J Sound Vib, 2022, 529: 116955.

[48] Yu W. Mathematical construction of a ReissnerCMindlin plate theory for composite laminates. Int J Solids Struct, 2005, 42(26): 6680-6699.

[49] Rao M V P, Harursampath D, Renji K. Prediction of inter-laminar stresses in composite honeycomb sandwich panels under mechanical loading using Variational Asymptotic Method. Compos Struct, 2012, 94(8): 2523-2537.

[50] Honda S, Narita Y. Vibration analysis and optimization of sandwich composite with curvilinear fibers[C]//Journal of Physics: Conference Series. IOP Publishing, 2016, 744(1): 012020.

[51] Honda S, Narita Y. Natural frequencies and vibration modes of laminated composite plates reinforced with arbitrary curvilinear fiber shape paths. J Sound Vib, 2012, 331(1): 180-191.

[52] Ribeiro P, Akhavan H, Teter A, et al. A review on the mechanical behaviour of curvilinear fibre composite laminated panels. J Compos Mater, 2014, 48(22): 2761-2777.

[53] Narita Y. Layerwise optimization for the maximum fundamental frequency of laminated composite plates. J Sound Vib, 2003, 263(5): 1005-1016.

[54] Vescovini R, Dozio L. A variable-kinematic model for variable stiffness plates: Vibration and buckling analysis. Compos Struct, 2016, 142: 15-26.

The highlights of this article are:

- VAM is extended to establish 2D-AEM of CSP-ARH, and verified by comparison with 3D-FEM.
- 2D-AEM reduces the DOFs of the CSP-ARH and improves calculation efficiency.
- The PSO algorithm is applied to optimize the structural parameters of CSP-ARH.
- The buckling and free vibration behaviors of CSP-ARH and CSP-ARH-CLF are investigated using 2D-AEM.
- Optimizing the direction of curved fibers can further improve the mechanical properties of CSP-ARH-CLF.